

This item is likely protected under Title 17 of the U.S. Copyright Law. Unless on a Creative Commons license, for uses protected by Copyright Law, contact the copyright holder or the author.

Access to this work was provided by the University of Maryland, Baltimore County (UMBC) ScholarWorks@UMBC digital repository on the Maryland Shared Open Access (MD-SOAR) platform.

Please provide feedback

Please support the ScholarWorks@UMBC repository by emailing scholarworks-group@umbc.edu and telling us what having access to this work means to you and why it's important to you. Thank you.

The Complex X-ray Obscuration Environment in the Radio Loud Type 2 Quasar 3C 223

STEPHANIE M. LAMASSA,¹ TAHIR YAQOUB,^{2,3} PANAYIOTIS TZANAVARIS,^{4,5,2} POSHAK GANDHI,^{6,7} TIMOTHY HECKMAN,⁸
GEORGE LANSBURY,⁹ AND ANETA SIEMIGINOWSKA¹⁰

¹*Space Telescope Science Institute, 3700 San Martin Drive, Baltimore, MD, 21218, USA*

²*CRESSST, University of Maryland Baltimore County, 1000 Hilltop Circle, Baltimore, MD, 21250, USA*

³*NASA/Goddard Spaceflight Center, Mail Code 662, Greenbelt 20771, USA*

⁴*University of Maryland Baltimore County, 1000 Hilltop Circle, Baltimore, MD, 21250, USA*

⁵*Laboratory for X-ray Astrophysics, NASA/Goddard Spaceflight Center, Mail Code 662, Greenbelt 20771, USA*

⁶*School of Physics & Astronomy, University of Southampton, Highfield, Southampton SO17 1BJ, UK*

⁷*Inter-University Centre for Astronomy & Astrophysics, Post Bag 4, Ganeshkhind, Pune 411007, India*

⁸*Center for Astrophysical Sciences, Department of Physics & Astronomy, The Johns Hopkins University, Baltimore, MD 21218, USA*

⁹*European Southern Observatory, Karl-Schwarzschild str. 2, D-85748 Garching bei München, Germany*

¹⁰*Center for Astrophysics, Harvard and Smithsonian, 60 Garden St., Cambridge, MA 02138, USA*

ABSTRACT

3C 223 is a radio loud, Type 2 quasar at $z = 0.1365$ with an intriguing *XMM-Newton* spectrum that implicated it as a rare, Compton-thick ($N_{\text{H}} \gtrsim 1.25 \times 10^{24} \text{ cm}^{-2}$) active galactic nucleus (AGN). We obtained contemporaneous *XMM-Newton* and *NuSTAR* spectra to fit the broad-band X-ray spectrum with the physically-motivated MYTORUS and BORUS02 models. We confirm earlier results that the obscuring gas is patchy with both high (though not Compton-thick) levels of obscuration ($N_{\text{H}} > 10^{23} \text{ cm}^{-2}$) and gas clouds with column densities up to an order of magnitude lower. The spectral fitting results indicate additional physical processes beyond those modeled in the spectral grids of MYTORUS and BORUS02 impact the emergent spectrum: the Compton-scattering region may be extended beyond the putative torus; a ring of heavy Compton-thick material blocks most X-ray emission along the line of sight; or the radio jet is beamed, boosting the production of Fe K α line photons in the global medium compared with what is observed along the line of sight. We revisit a recent claim that no radio loud Compton-thick AGN have yet been conclusively shown to exist, finding three reported cases of radio loud AGN with global average (but not line-of-sight) column densities that are Compton-thick. Now that it is possible to separately determine line-of-sight and global column densities, inhomogeneity in the obscuring medium has consequences for how we interpret the spectrum and classify an AGN as “Compton-thick.”

Keywords: active galaxies, high energy astrophysics, X-ray active galactic nuclei, quasars, radio loud quasars, radio jets, Fanaroff-Riley radio galaxies, X-ray astronomy

1. INTRODUCTION

The hidden side of supermassive black hole accretion has long captivated the astronomy community. The observational properties of active galactic nuclei (AGN) are diverse (Hickox & Alexander 2018), but can trace their origins to accretion onto a black hole that ionizes gas both near and far (in the Broad Line Region and Narrow Line region, respectively). A corona of hot gas

above and below the accretion disk is thought to inverse Compton scatter optical and ultraviolet photons from the disk to X-ray energies (Haardt & Maraschi 1991). In some AGN, a radio jet is launched from either the inner edges of the accretion disk (Blandford & Payne 1982) or via a mechanism involving magnetic fields tapping into the black hole spin energy (Blandford & Znajek 1977). According to AGN unified models, a “torus” of gas and dust surrounds the accretion disk, absorbing photons along the equatorial plane but allowing radiation from the accretion disk to escape along the polar axis (Antonucci 1993; Urry & Padovani 1995; Netzer 2015). Dust in the torus absorbs the optical to ultraviolet light ema-

nating from the accretion disk while gas, which can exist within the dust sublimation zone, absorbs and scatters X-ray photons produced by the corona. When the column density of this obscuring gas reaches levels where it becomes optically thick to Compton scattering ($N_{\text{H}} \geq 1/(1.2 \times \sigma_T) \simeq 1.25 \times 10^{24} \text{ cm}^{-2}$)¹, the AGN is defined as “Compton-thick.”

Compton-thick AGN are an interesting population that, though difficult to detect, nevertheless leave their imprint on the cosmic energy budget and cannot be dismissed as mere curiosities. Studies of the cosmic X-ray background reveal an unresolved component: after integrating the emission of resolved X-ray sources, excess emission remains (e.g., Worsley et al. 2005). A sizeable portion of Compton-thick AGN have been invoked to account for this excess (Ueda et al. 2003). The exact fraction of accretion enshrouded by Compton-thick material is still a matter of debate as different model assumptions about the X-ray spectra of AGN and observational biases of X-ray surveys can lead to different results. Currently the Compton-thick AGN fraction has been quoted to be anywhere from $\sim 9 - 50\%$ (Gilli et al. 2007; Treister et al. 2009; Akylas et al. 2012; Ueda et al. 2014; Ricci et al. 2015; Ananna et al. 2019) though these studies do not incorporate models where the line-of-sight and global column densities can differ significantly as reported in detailed studies of individual AGN (e.g., Yaqoob et al. 2015; LaMassa et al. 2016, 2017; Baloković et al. 2018; Tzanavaris et al. 2019, 2021; Zhao et al. 2021).

Compton-thick AGN may represent a transient phase in supermassive black hole evolution. For instance, the major merger paradigm of black hole growth predicts a phase of rapid black hole growth nestled within high-to-Compton-thick levels of obscuration, followed by AGN outflows that evacuate the cocoon of absorbing material (Sanders et al. 1988; Hopkins et al. 2006, 2008). A better understanding of the Compton-thick population, and the complex distribution of obscuring gas, can then shed light about a key phase of galaxy and black hole co-evolution.

Radio jets launched from an AGN also play a role in shaping the environment in which an AGN lives, both on galactic and extragalactic scales (see Fabian 2012, and references therein). Recently, Ursini et al. (2018) claimed that no bona-fide Compton-thick radio loud AGN have demonstrably been identified. Though a handful of radio loud Compton-thick *candidates* have

been proposed (Panessa et al. 2016), the column densities for these sources were estimated from X-ray spectral fits below 10 keV, often using simplified spectral models. Simple absorbed power law models that assume a screen of extinction often fail to capture the inherent complexity of AGN spectra and can under-estimate the obscuring column density when the spectrum is dominated by scattered AGN emission that leaks through the torus (Turner et al. 1997; Turner & Miller 2009; Winter et al. 2009; LaMassa et al. 2009, 2011). Other clues can point to heavy levels of obscuration, including a depressed observed 2-10 keV X-ray flux when normalized to the intrinsic AGN luminosity (Bassani et al. 1999; Heckman et al. 2005; Panessa et al. 2006; LaMassa et al. 2009, 2011; Jia et al. 2013), and a large Fe K α equivalent width ($\text{EW} \gtrsim 1 \text{ keV}$) due to the suppression of the absorbed continuum against which the Fe K α line (formed via fluorescence within the obscuring matter) is measured (Krolik et al. 1994; Ghisellini et al. 1994; Matt et al. 1996), though weaker Fe K α lines are sometimes observed in Compton-thick AGN (see Gandhi et al. 2017; Boorman et al. 2018).

Even when more complex models are invoked that self-consistently account for the effects of Compton-scattering and therefore measure the column density more accurately, spectra below 10 keV only tell part of the story. Spectra above 10 keV are necessary to observe the Compton hump, thereby constraining the spectral fit. Such broad band spectral fitting (0.5-50 keV) sometimes paints very different pictures about the column density and geometry of the X-ray obscuring medium than when only data below 10 keV are fitted (see, e.g., LaMassa et al. 2019). Indeed, Ursini et al. (2018) point out that when including $>10 \text{ keV}$ *NuSTAR* data in the spectral fitting of three radio loud Compton-thick candidates, none of them had measured column densities within the Compton-thick regime.

Here we explore the X-ray properties of 3C 223, a radio loud, Type 2 (i.e., optically obscured) quasar at $z = 0.1365$. It is a Fanaroff-Riley class II (FR II, radio lobe dominated; Fanaroff & Riley 1974), High Excitation Radio Galaxy (strong narrow optical emission lines; Hine & Longair 1979) with a projected linear size larger than 1 Mpc where the age of the radio source is estimated to be $72 \pm 4 \text{ Myr}$ (Orrù et al. 2010). Reyes et al. (2008) selected this source as a Type 2 quasar on the basis of its high [O III] luminosity. LaMassa et al. (2014) presented 3C 223² as a Compton-thick candidate, where

¹ σ_T is the Thompson cross-section and the factor of 1.2 accounts for the contributions of electrons from both Hydrogen and Helium.

² 3C 223 was referred to by its SDSS identifier, J093952.74+355358.0, in Reyes et al. (2008), Jia et al. (2013), and LaMassa et al. (2014).

its unusual X-ray spectral properties observed by *XMM-Newton* were highlighted. This source boasted a large Fe K α EW (~ 500 eV, Jia et al. 2013) while lacking an accompanying spectral curvature between 2 - 6 keV associated with Compton-thick reprocessing. LaMassa et al. (2014) posited that the spectral features were a clue that the X-ray reprocessing medium was non-uniform, with a global average column density that is Compton-thin (consistent with the observed lack of spectral curvature between 2 - 6 keV), but a line-of-sight column density that is Compton-thick but with a low covering factor. They proposed that a “ring” of Compton-thick obscuration could suppress the continuum just enough around the Fe K α line to boost the EW, but not impose the spectral curvature expected from a medium that is globally Compton-thick. They found a good fit to the *XMM-Newton* spectrum of 3C 223 using the physically motivated MYTORUS model (Murphy & Yaqoob 2009) in a configuration where they decoupled the line-of-sight column density ($N_{\text{H,los}}$) from the global average column density ($N_{\text{H,global}}$). They measured a Compton-thick line-of-sight column density ($N_{\text{H,los}} > 1.7 \times 10^{24} \text{ cm}^{-2}$) and a Compton-thin global average column density ($N_{\text{H,global}} = 1.4 \times 10^{23} \text{ cm}^{-2}$), supporting the hypothesis that a ring of Compton-thick gas clouds were embedded in a global Compton-thin medium.

Could 3C 223 then be an exception to the trend reported by Ursini et al. (2018)? We obtained contemporaneous *NuSTAR* and *XMM-Newton* data to find out. In Section 3.3, we describe the results from fitting the *XMM-Newton* and *NuSTAR* spectra with the MYTORUS and BORUS02 models, with a summary of rejected model fits described in the Appendix. In Section 4.1, we explore possible physical scenarios that can explain the X-ray fitting results. From the absorption corrected X-ray luminosity and [O III] luminosity, we estimate the bolometric luminosity and Eddington ratio of 3C 223 (Section 4.3) and compare that with amount of energy carried by the radio jet in Section 4.4. In Section 4.5, we compare 3C 223 with other [O III]-defined Type 2 quasars observed by *NuSTAR*. Finally, we revisit the question of whether there is a lack of radio loud Compton-thick AGN in Section 4.6. Throughout the paper, we assume a cosmology where $H_0 = 67.7 \text{ km/s/Mpc}$ and $\Omega_m = 0.307$ (Planck Collaboration et al. 2016).

2. X-RAY OBSERVATIONS AND DATA REDUCTION

XMM-Newton observed 3C 223 in 2001 October for 35 ks (PI: Birkinshaw, ObsID: 0021740101) and in 2019 November for 48 ks (PI: LaMassa; ObsID: 0852580101). *XMM-Newton* is sensitive to X-ray light with energies

between 0.5 - 10 keV and has 3 co-aligned detectors: PN, MOS1, and MOS2. We processed the data from all three detectors with the *XMM-Newton* Science Analysis System (SAS) v.1.3. We applied standard filtering to the data and assigned good time intervals by inspecting the light curves and using a count rate threshold to remove periods of flaring from the particle background. As shown in Table 1, this filtering leaves us with a net exposure of about 15-19 ks and 17-23 ks for the observations from 2001 and 2019 respectively.

We extracted spectra from the PN, MOS1, and MOS2 detectors using a circular aperture with a radius of $30''$ ($\sim 75 \text{ kpc}$) centered on the X-ray source. The background counts for all three detectors were extracted from a source-free circular region with a $75''$ radius near the AGN. The net counts summed among the three detectors for the observations from 2001 and 2019 are 1526.6 and 1391.5, respectively. Croston et al. (2004) identified X-ray emission from the radio lobes of 3C 223 in the 2001 *XMM-Newton* observation of this source which they attributed to inverse Compton scattering from cosmic microwave background photons within the lobes. Since the purpose of our investigation is to understand the circumnuclear obscuration environment, we took care to extract the source and background spectra from regions that did not overlap the X-ray lobes reported by Croston et al. (2004).

3C 223 was observed with *NuSTAR* in 2019 November (PI: LaMassa, ObsID: 60501020002) for 48.5 ks. *NuSTAR* is the first hard X-ray ($> 10 \text{ keV}$) focusing X-ray observatory and has two detectors in the focal plane (FPMA and FPMB) which are sensitive to energies between 3 - 79 keV (Harrison et al. 2013). We processed the data with the NUPipeline package of the *NuSTAR* Data Analysis Software (NustardAS) v.2.0.0 using CALDB v.20210701. We extracted spectra separately from both modules, using a circular source region with a $45''$ ($\sim 110 \text{ kpc}$) radius and a circular background region of radius $90''$ chosen to be on the same quadrant of the detector as the source to best sample the local background. Between the two modules, we detected 1070.6 net X-ray photons from the *NuSTAR* observation of 3C 223.

We grouped the spectra using FTGROUPPHA to have a minimum signal-to-noise ratio (S/N) in the background-subtracted spectra of $S/N = 3$ for the *XMM-Newton* spectra and $S/N = 2$ for the *NuSTAR* spectra. This binning allows for adequate resolution around the Fe K α line in the *XMM-Newton* spectra, while the lower S/N threshold for the *NuSTAR* spectra allows for a spectral bin between 20 - 30 keV.

Table 1. X-ray Observing Log of 3C 223

Observatory	Observation Date	Observation ID	Exposure Time (ks) ^a	Net Counts
<i>XMM-Newton</i>	2001-10-27	0021740101	34.9	1526.6
PN/MOS1/MOS2			15.7/18.2/19.4	890.6/328.5/307.5
<i>XMM-Newton</i>	2019-11-09	0852580101	48.0	1391.5
PN/MOS1/MOS2			17.2/23.1/23.5	761.5/316.7/313.3
<i>NuSTAR</i>	2019-11-10	6050102000	48.5	1070.6
FPMA/FPMB			48.5/48.2	517.4/553.2

^aThe top row reports the total duration of the X-ray observations. The second row reports the net exposure time after filtering the data and applying the good time intervals (GTI). Since the data from each detector were reduced independently, there are different GTIs for each dataset, resulting in different net exposure times.

3. X-RAY SPECTRAL FITTING

We used XSPEC v.12.11.1 (Arnaud 1996) to fit the *XMM-Newton* spectra from 2001 and 2019 simultaneously with the *NuSTAR* spectrum from 2019, using χ^2 as the fit statistic. All reported errors represent the 90% confidence interval ($\Delta\chi^2=2.706$). As we discuss in detail in Appendix A, we find no evidence for spectral variability among the X-ray observations of 3C 223.

3.1. Self-Consistent Treatment of X-ray Reprocessing

3.1.1. MYTORUS Model

We fitted the spectra of 3C 223 with MYTORUS, a physically motivated X-ray model that self-consistently treats the reprocessing of X-ray emission in obscured AGN ($N_{\text{H}} > 10^{22} \text{ cm}^{-2}$; Murphy & Yaqoob 2009). The MYTORUS model is available as XSPEC table models that are derived from Monte Carlo simulations that calculate the effects of the transmitted continuum, Compton scattered component, and Fe $K\alpha$ and Fe $K\beta$ fluorescent line emission over a range of input parameters to produce observed X-ray spectra. The elemental abundances are the solar values from Anders & Grevesse (1989) with photoelectric absorption cross-sections from Verner et al. (1996).

The default configuration of the MYTORUS model assumes a geometry where the X-ray reprocessor is “doughnut-shaped” (azimuthally symmetric), and has a fixed covering factor of 0.5, corresponding to an opening angle of 60° . In this default configuration, any inclination angle greater than 60° intersects the torus while any smaller inclination angle corresponds to a face-on orientation that allows an unimpeded view of the X-ray emitting region. Modeling the intrinsic AGN continuum as a powerlaw, the allowed ranges of the spectral slope within the MYTORUS model are $1.4 \leq \Gamma \leq 2.6$.

The allowed equivalent hydrogen column densities range from 10^{22} cm^{-2} - 10^{25} cm^{-2} , and in this default, “coupled” configuration, the measured column density reflects the equatorial column density ($N_{\text{H,equatorial}}$), i.e., the amount of Hydrogen measured through the diameter of the torus cross-section.

However, the X-ray reprocessor need not be uniform, and mounting evidence indicates that the X-ray reprocessor is not always homogeneous, with significantly different global average column densities from those measured along the line of sight (Yaqoob et al. 2015; LaMassa et al. 2016, 2017; Baloković et al. 2018; Tzanavaris et al. 2019, 2021; Zhao et al. 2021). Eclipsing events that have been observed in the X-ray spectra of some AGN offer clues that discrete clouds of gas can transit into and out of the line of sight, manifesting significant changes in the observed column density on the timescale of days to years (McKernan & Yaqoob 1998; Risaliti et al. 2002, 2005; Rivers et al. 2015; Marinucci et al. 2016; Ricci et al. 2016). The decoupled MYTORUS model configuration offers the flexibility to disentangle the global column density ($N_{\text{H,global}}$) from the line-of-sight column density ($N_{\text{H,los}}$) (see Yaqoob 2012; LaMassa et al. 2014; Tzanavaris et al. 2019). The geometry or covering fraction of the X-ray reprocessor can not necessarily be constrained by the decoupled MYTORUS model configuration, but measurements of the independent column densities indicate whether the obscuring medium is patchy or uniform.

For both the coupled and decoupled MYTORUS configurations, the high-level model set-up in XSPEC is the

same:

$$\begin{aligned} \text{model} = & \text{const}_1 \times \text{phabs} \times \\ & (z\text{pow}_1 \times \text{etable}\{\text{mytorus_Ezero_v00.fits}\} + \\ & \text{const}_2 \times \text{atable}\{\text{mytorus_scatteredH200_v00.fits}\} + \\ & \text{const}_3 \times \\ & \text{atable}\{\text{mytl_V000010nEp000H200_v00.fits}\}) \end{aligned}$$

where ZPOW_1 models the intrinsic AGN powerlaw emission; MYTORUS_EZERO_V00.FITS, MYTORUS_SCATTEREDH200_V00.FITS, and MYTL_V000010NEP000H200_V00.FITS model the attenuation of the transmitted AGN continuum, Compton scattered emission, and fluorescent line emission, respectively; PHABS is frozen to the Galactic column density ($N_{\text{H,Galactic}} = 1.46 \times 10^{20} \text{ cm}^{-2}$);³ and CONST_1, CONST_2, and CONST_3 are constants to model the cross-instrument normalization, relative normalization between the transmitted and Compton scattered components (A_S), and relative normalization between the transmitted and fluorescent line emission component (A_L , which is always linked to A_S), respectively. The column density and inclination angle associated with the Compton scattered and fluorescent line emission components are always tied to the same value.

For the coupled MYTORUS configuration, all torus components (i.e., $N_{\text{H,equatorial}}$ and inclination angle) are linked between the transmitted, and Compton scattered/fluorescent line models. In the decoupled configuration, the column densities are fitted independently between the transmitted component and the Compton scattered/fluorescent line emission. The inclination angle of the X-ray reprocessor associated with the transmitted component is frozen to 90° so that the measured column density is that along the line of sight ($N_{\text{H,los}}$). The inclination angle of the X-ray reprocessor associated with the Compton scattered and fluorescent line emission components is frozen to 0° to mimic face-on reflection via scattering off the back-side of the torus without further interaction with intervening matter. Here, the fitted column density reflects the global average column density ($N_{\text{H,global}}$).

3.1.2. BORUS02 Model

The BORUS02 model (Baloković et al. 2018) allows the global average column density to be fitted independently from the line-of-sight column density, similar to the MYTORUS model in decoupled mode. Unlike

the MYTORUS model, this independence in fitted column densities is achieved by adding an additional cutoff powerlaw model component (CUTOFFPL) to the overall model that is distinct from the BORUS spectral templates calculated via radiative transfer codes from which the BORUS02 XSpec table model is defined. Self-consistency between the absorbed power law component and BORUS02 model is assumed by linking the parameters of the powerlaw model to the BORUS02 model.

$$\begin{aligned} \text{model} = & \text{const}_1 \times \text{phabs} \times \\ & (\text{atable}\{\text{borus02_v170323a.fits}\} + \\ & z\text{phabs} \times \text{cabs} \times \text{cutoffpl}) \end{aligned}$$

Here, the first PHABS component is frozen to the Galactic column density (as above) while the second PHABS component is linked to the CABS column density, which is an absorption model that accounts for Compton-scattering.

BORUS02 also fits the covering factor of the torus ($CF_{\text{tor}} = \cos(\theta_{\text{tor}})$, where θ_{tor} is the torus opening angle), which is the fraction of the sky obscured by the torus as seen by the X-ray source. The covering factor ranges from 10% to 100% (i.e., completely covered). However, as noted in LaMassa et al. (2019), it is unclear how this covering factor relates to the line-of-sight column density as the latter is parameterized by an additive model component that is independent from the radiative transfer calculations used to derive the BORUS02 spectral template grid in which CF_{tor} is measured. An advantage of the BORUS02 model is that the iron abundance (A_{Fe}) can be fitted as a free parameter, allowing us to test whether a super-solar iron abundance can partially explain the enhanced iron emission with respect to the continuum seen in the *XMM-Newton* spectra (Jia et al. 2013; LaMassa et al. 2014). The BORUS02 energy lower energy range terminates at 1 keV, unlike the MYTORUS model which is valid to 0.6 keV.

3.2. Modeling the Soft X-ray Emission: Scattered AGN Light or Jet Emission?

Excess emission above an absorbed power law (representing the attenuated transmitted AGN continuum) is apparent at soft X-ray energies ($< 2 \text{ keV}$) for many AGN, and can originate from different components. This emission can represent the scattering of the intrinsic AGN continuum off of free electrons in distant, optically thin material (Winter et al. 2009; Turner & Miller 2009; LaMassa et al. 2009, 2011); thermal emission from the host galaxy (Turner et al. 1997; LaMassa et al. 2012) or unresolved photoionized emission due to the AGN (e.g., Guainazzi & Bianchi 2007); or non-thermal unre-

³ Galactic column density derived from Colden which is hosted by the *Chandra* X-ray Observatory science center: <https://cxc.harvard.edu/toolkit/colden.jsp>

solved jet emission (Hardcastle et al. 2006, 2009). In low-resolution (i.e., non-grating, non-microcalorimeter) X-ray spectra from CCD detectors, thermal emission from star-formation or AGN photoionization can be well described with thermal X-ray models like APEC, where high resolution spectroscopy is necessary to definitively pinpoint the physical origins of the soft emission. Though the soft X-ray spectra of radio loud AGN can often be well fitted by either of the non-thermal models, Hardcastle et al. (2006, 2009) argue that the soft X-ray emission in radio loud AGN has its physical origins in an X-ray jet due to the strong correlation between the nuclear radio (jet) emission and the soft X-ray luminosity.

Both a partial covering and a jet-origin scenario are described by powerlaw models, so we added a powerlaw model to the above model set-ups to accommodate the soft X-ray spectrum below 2 keV. This powerlaw emission is attenuated by $N_{\text{H,Galactic}}$ but is unaffected by the circumnuclear absorption that suppresses the AGN emission.

In the partial covering model, this second power law model describes AGN emission that is scattered into the line of sight. It therefore has the same power law slope (Γ) and normalization as the primary power law model, where this consistency is enforced by linking these parameters together in the spectral fitting. A constant multiplicative factor was introduced as a free parameter before the second power law model to parameterize the scattering fraction (f_{scatt}). To describe soft X-ray emission from a jet, the spectral slope and normalization of the second power law component are fitted independently from the primary power law, and no extra multiplicative factor is included in the fitting. Hardcastle et al. (2009) find that the slope of the unabsorbed power law component (which they ascribe to the jet) varies from $1.2 \lesssim \Gamma \lesssim 2.4$, with a median value of $\Gamma = 1.6$ (calculated from the fits where Γ to the unabsorbed power law was a free parameter in the modeling). This median powerlaw slope is somewhat harder than the canonical AGN slope of $1.7 < \Gamma < 1.9$ (e.g., Tozzi et al. 2006), but there is a wide range of fitted values for the assumed jet component, so there is not a typical power law slope that cleanly distinguishes AGN coronal emission from jet emission.

Since the MYTORUS model is sensitive to lower energies than the BORUS02 model, we use the former model to try to distinguish between a jet or scattered AGN light origin for the soft X-ray emission. With the BORUS02 model, we simply accommodate the excess between 1 - 2 keV with a cutoff powerlaw model modified by a multiplicative factor to parameterize f_{scatt} .

3.3. X-ray Fitting Results

We found that the X-ray spectra of 3C 223 are best-fit by the MYTORUS model in the decoupled mode where the relative normalization between the transmitted and Compton scattered emission (A_S) is fitted as a free parameter (see Appendix B for a discussion of MYTORUS fit results that we rejected) and by the BORUS02 model. The fitted parameters are summarized in Tables 2 - 3, and the fitted spectra and model components are shown in Figures 1 - 2. The BORUS02 model finds a slightly enhanced iron abundance ($A_{\text{Fe}} = 2.2^{+1.8}_{-0.9}$) and the covering factor is not well constrained ($CF_{\text{tor}} > 0.29$).

At first glance, the model fits imply contradictory results. The MYTORUS scattered AGN model finds a much higher column density along the line of sight ($N_{\text{H,los}} = 0.56^{+2.4}_{-1.9} \times 10^{24} \text{ cm}^{-2}$) than the global average column density ($N_{\text{H,global}} = 0.07^{+0.03}_{-0.02} \times 10^{24} \text{ cm}^{-2}$), while the opposite is found from the MYTORUS jet model ($N_{\text{H,los}} = 0.08^{+0.04}_{-0.02} \times 10^{24} \text{ cm}^{-2}$; $N_{\text{H,global}} = 0.80^{+0.48}_{-0.33} \times 10^{24} \text{ cm}^{-2}$) and BORUS02 model ($N_{\text{H,los}} = 0.16^{+0.05}_{-0.03} \times 10^{24} \text{ cm}^{-2}$; $N_{\text{H,global}} = 0.87^{+1.13}_{-0.68} \times 10^{24} \text{ cm}^{-2}$). The models also disagree as to the dominant source of emission between $\sim 2 - 5$ keV, with the MYTORUS scattered AGN model favoring a reflection-dominated spectrum while the MYTORUS jet model finds a transmission dominated-spectrum. The BORUS02 model is transmission-dominated above 3 keV but the scattered AGN component drives the spectrum below 3 keV.

The fitted power law slope of the AGN continuum from the MYTORUS scattered AGN model, $\Gamma = 1.91^{+0.33}_{-0.27}$, is typical of radiatively efficient, radio quiet AGN ($\Gamma \sim 1.9$; Reeves & Turner 2000, and references therein), while some past studies indicate that radio loud AGN tend to have flatter spectra ($\Gamma \sim 1.6$). The fitted AGN spectral slope for both the MYTORUS jet model and BORUS02 model are harder than that measured with the MYTORUS scattered AGN model, but a clear dichotomy in the spectral hardness between radio quiet and radio loud AGN is not always observed (e.g., Sambruna & Eracleous 2001; Hardcastle et al. 2006, 2007, 2009), meaning that we can not use spectral hardness alone to reject the MYTORUS scattered AGN model. Furthermore, the best fit AGN spectral slope pegged at the minimum allowed value ($\Gamma_{\text{limit}} = 1.4$) in the MYTORUS jet model and BORUS02 model, raising questions about the reliability of these model fits.

Here is where the models agree: the obscuring medium reprocessing the X-ray emission from the AGN in 3C 223 is non-homogeneous, with up to an order of magnitude difference between the line-of-sight and global average column density. The column density of the obscuring

gas is quite high, though not Compton-thick, reaching levels above 10^{23} cm^{-2} . And a closer inspection of the fit parameters reveal that extra physics is at play to boost the soft X-ray spectrum beyond what can be accounted for in the radiative transfer codes used to define the MYTORUS and BORUS02 model grids. The normalization between the transmitted and Compton-scattered components of both MYTORUS models is constrained to be several times greater than unity ($A_S \sim 5 - 6$) and the AGN “scattering fraction” found by the BORUS02 model ($f_{\text{scatt}} = 27^{+5}_{-3}\%$) is much higher than the $<1\text{-}3\%$ typically found in AGN (Winter et al. 2009; Turner & Miller 2009; LaMassa et al. 2009, 2011) and is unphysical (Buchner et al. 2019). In fact, this high scattering fraction, and measured column densities, are consistent with those found from the MYTORUS scattered AGN model using MYTORUS in decoupled mode and with A_S frozen to unity (see Appendix B), so there is a degeneracy between accommodating the $<3 \text{ keV}$ part of X-ray spectrum with an unphysical scattering fraction or an elevated normalization between the transmitted and Compton-scattered emission. Since we allow iron abundance to be a free parameter in the spectral fitting, we can rule out enhanced iron abundances as a main driver for an elevated normalization between the Compton-scattered and transmitted emission.

To test whether excess unresolved thermal emission at soft energies could give rise to the high scattering fraction/elevated normalization, we included an APEC component for this potential emission in our MYTORUS scattered AGN model. The fit improved marginally ($\chi^2=330.2$ for 408 degrees of freedom), but the best fit A_S was even higher than when this component was not included ($A_S = 14^{+15}_{-8}$). When adding the APEC component to the MYTORUS jet model, the APEC model parameters were unconstrained. We thus conclude that high relative normalization between the transmitted and Compton scattered component is not due to unresolved host galaxy emission boosting the spectrum at soft energies.

4. DISCUSSION

4.1. *Insight into the Obscuring Medium: Inhomogeneity and Physical Implications of Deviations from Model Assumptions*

3C 223 joins the list of obscured AGN whose obscuring medium is shown via broad band X-ray spectral coverage (0.5 - 30 keV), where enough counts are garnered to permit use of physically motivated spectral models, to be more complicated than that assumed by simplistic models where the torus is homogeneous and uniform (Yaqoob et al. 2015; Baloković et al. 2018; Tzanavaris

Table 2. Decoupled MYTORUS Fit Parameters^a

Parameter	Scattered AGN	Jet
Γ_{AGN}	$1.91^{+0.33}_{-0.27}$	<1.62
Power law norm - AGN (10^{-4})	$6.05^{+14.9}_{-3.95}$	$0.57^{+0.35}_{-0.10}$
Γ_{Jet}	...	$1.83^{+0.24}_{-0.23}$
Power law norm - Jet (10^{-4})	...	0.26 ± 0.02
$N_{\text{H,los}}$ (10^{24} cm^{-2})	$0.56^{+0.24}_{-0.19}$	$0.08^{+0.04}_{-0.02}$
$N_{\text{H,global}}$ (10^{24} cm^{-2})	$0.07^{+0.03}_{-0.02}$	$0.80^{+0.48}_{-0.33}$
A_S^b	$6.4^{+3.8}_{-3.1}$	$5.1^{+2.3}_{-1.8}$
f_{scatt} (10^{-2})	$3.9^{+7.4}_{-2.8}$...
χ^2 (dof)	338.8 (395)	336.7 (394)
X-ray luminosities ^c		
$\text{Log}(L_{2-10\text{keV,observed}} \text{ erg s}^{-1})$	43.27 ± 0.14	$43.26^{+0.21}_{-0.08}$
$\text{Log}(L_{10-40\text{keV,observed}} \text{ erg s}^{-1})$	43.70 ± 0.14	$43.79^{+0.21}_{-0.08}$
$\text{Log}(L_{2-10\text{keV,intrinsic}} \text{ erg s}^{-1})$	$43.87^{+0.74}_{-0.69}$	$43.22^{+0.21}_{-0.25}$

^aBest fit parameters from modeling the *XMM-Newton* and *NuSTAR* spectra of 3C 223 with the MYTORUS model in decoupled mode, where the line-of-sight column density ($N_{\text{H,los}}$) of the X-ray obscurer is fitted independently from the global average column density ($N_{\text{H,global}}$). The soft emission (0.5 - 2 keV) was modeled assuming it originates from AGN emission scattered into our line of sight (“Scattered AGN” column), or that it emanates from the base of an X-ray jet (“Jet” column), with a powerlaw spectral index (Γ_{jet}) independent of the primary AGN component (Γ_{AGN}).

^bNormalization between the transmitted AGN continuum and the Compton scattered and fluorescent line emission.

^cX-ray luminosities refer to the AGN luminosities and are derived from the average X-ray fluxes measured by the spectral model for each instrument. The errors on the observed luminosities are based on propagating errors in the powerlaw normalization. The intrinsic luminosity is calculated from an absorption-corrected powerlaw model with Γ and the normalization set to the best-fit values from spectral fitting. The errors on the intrinsic luminosity account for the range of possible luminosities based on the errors in the normalization and spectral index of the powerlaw model.

et al. 2021). The X-ray spectra of 3C 223 require the presence of heavy attenuation ($> 10^{23} \text{ cm}^{-2}$) along with gas clouds with column densities up to an order of magnitude lower, though how this gas is distributed depends on the spectral model. Studies that purport to trace the evolution of obscured supermassive black hole accretion by analyzing the unresolved cosmic X-ray background rely on models that assume a uniform column density for all sight-lines (Gilli et al. 2007; Treister et al. 2009; Akylas et al. 2012; Ueda et al. 2014; Ananna et al. 2019), oversimplifying our emergent picture of the inhomogeneous reprocessing medium in AGN where the global

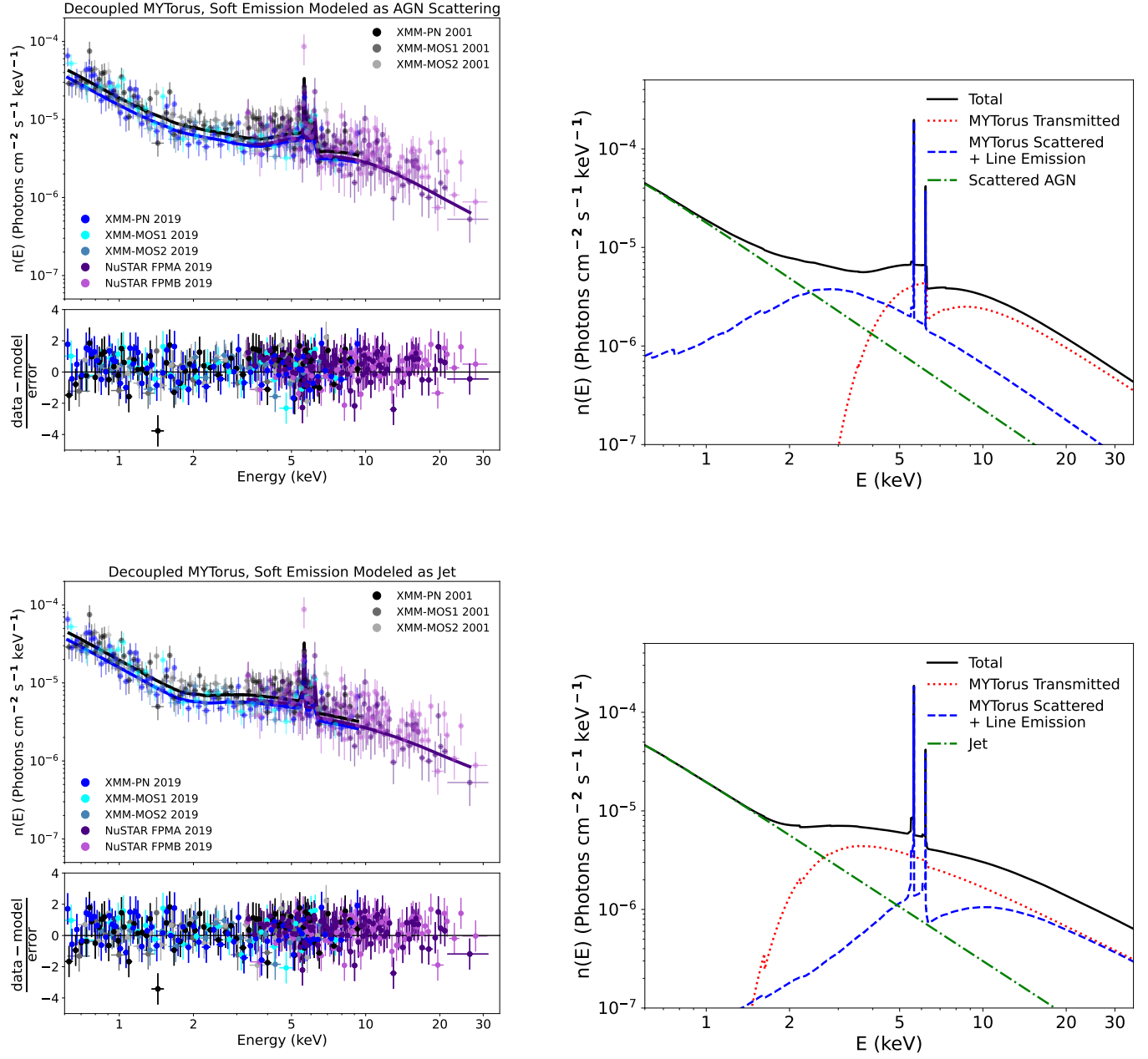


Figure 1. *Left:* Decoupled MYTORUS fit to the unfolded *XMM-Newton* and *NuSTAR* spectra of 3C 223, modeling the soft X-ray emission (0.5 - 2 keV) as scattered AGN light (top) and as jet emission (bottom). *Right:* Best-fit model, with individual components plotted separately for illustrative purposes. Both models allow the normalization between the transmitted AGN continuum and Compton scattered/fluorescent line emission to be a free parameter. The models provide nearly identical fits to the spectra, but with different intrinsic physical properties. With the scattered AGN model, the X-ray spectrum is reflection dominated between 2 - 5 keV while it is transmission dominated above 2 keV in the jet model.

Table 3. BORUS02 Fit Parameters

Parameter	Value
Γ	<1.50
Power law norm (10^{-4})	$0.69^{+0.02}_{-0.11}$
Inclination angle ($^{\circ}$)	>55
$N_{\text{H,los}}$ (10^{24} cm^{-2})	$0.16^{+0.05}_{-0.03}$
$N_{\text{H,global}}$ (10^{24} cm^{-2})	$0.87^{+1.13}_{-0.68}$
$CF_{\text{tor}}^{\text{a}}$	>0.29
A_{Fe}^{b}	$2.2^{+1.8}_{-0.9}$
f_{scatt} (10^{-2})	27^{+5}_{-3}
χ^2 (dof)	302.1 (348)
X-ray luminosities	
$\text{Log}(L_{2-10\text{keV,observed}} \text{ erg s}^{-1})$	$43.26^{+0.06}_{-0.01}$
$\text{Log}(L_{10-40\text{keV,observed}} \text{ erg s}^{-1})$	$43.79^{+0.06}_{-0.01}$
$\text{Log}(L_{2-10\text{keV,intrinsic}} \text{ erg s}^{-1})$	$43.30^{+0.01}_{-0.15}$

^a CF_{tor} refers to the torus covering factor which is defined as $\cos(\theta_{\text{tor}})$, where θ_{tor} is the torus opening angle. C_{tor} can range from 0.1 (low covering factor) to 1.0 (spherical coverage).

^b A_{Fe} is the fitted iron abundance relative to solar.

column density may be the more relevant parameter (see Yaqoob et al. 2015).

In the MYTORUS model, an A_{S} value near unity implies that the intrinsic AGN continuum is constant, or that the reprocessor responds to any changes in the continuum on time scales that are much less than the spectrum integration time. A value that deviates significantly from unity, and the high scattering fraction in the BORUS02 model, indicate that additional physical processes are impacting the observed spectrum, with some possibilities illustrated in Figure 3.

Variability can be one such cause. The 0.5-10 keV X-ray observations were taken between the years of 2001 through 2019, with no variability observed in these spectra (Appendix A). If time delays are responsible for the high A_{S} value, that could indicate that the intrinsic continuum might have been much brighter years before the first *XMM-Newton* observing epoch and that the reprocessing material has not yet responded to this change. Such a scenario, illustrated in Figure 3 (top left), would indicate that the physical scale of the Compton-scattering region is larger than the light-travel distance covered by the 18 year window of the *XMM-Newton* observations (~ 5.5 pc, which is larger than the putative torus). Detailed studies of nearby obscured

AGN show evidence that though the bulk of the emission related to X-ray reprocessing (e.g., Fe K α emission) is nuclear (e.g., Gandhi et al. 2015), a fraction of this emission is detected on scales beyond the several pc torus (e.g., NGC1068, ESO 428-G014, NGC 5643, NGC 7212, NGC 4388; Bauer et al. 2015; Fabbiano et al. 2017, 2018; Jones et al. 2020). With our chosen cosmology, the physical scale at $z = 0.1365$ is $2.5 \text{ kpc}''$, so our X-ray spectra sample physical sizes of $\sim 75 - 110$ kpc. The high A_{S} or f_{scatt} value could then indicate that a fraction of the Compton scattering is occurring within a region well within the ~ 100 kpc sampled by our X-ray spectra, but on scales larger than the light-travel distance of 5.5 pc (otherwise we would have observed spectral variability in the intrinsic continuum between *XMM-Newton* epochs or measured a relative normalization closer to unity).

Alternatively, the covering factor of the obscuring medium in 3C 223 may deviate significantly from 0.5. The X-ray spectral shape supports a geometry where the line of sight is obscured by just enough material to boost the Fe K α EW (EW $\sim 0.5 \pm 0.2$ keV, Jia et al. 2013) while not imparting a spectral curvature between 2 - 6 keV associated with Compton-thick obscuration. As suggested in LaMassa et al. (2014) and illustrated in the top right panel of Figure 3, perhaps there is a ring of clouds around the X-ray emitting source that are heavily Compton-thick (i.e., $N_{\text{H}} > 10^{26} \text{ cm}^{-2}$) blocking most of the light in the equatorial direction while the global distribution of clouds can “see” most of the X-ray source. A fitted normalization of ~ 5 -6 between the Compton-scattered/line emission and transmitted continuum can indicate that the matter along the line of sight is illuminated by $\sim 20\%$ of the X-ray luminosity that is intercepted and reprocessed by the global medium. We attempted to model the X-ray spectra with UXCLUMPY to 1) test for the presence of an inner Compton-thick ($N_{\text{H}} > 10^{25} \text{ cm}^{-2}$) ring of material and 2) measure the angular width of the obscuring clouds. However, the inner Compton-thick ring is constrained to be smooth so this model is unable to test our posited scenario as this requires a patchy ring with a covering factor of $\sim 80\%$. Our modeling with UXCLUMPY resulted in a fit that did a poorer job of accommodating the Fe K α complex compared with our best-fit MYTORUS model (Appendix C). And similar to the BORUS02 model, UXCLUMPY modeling results in an unphysical scattering fraction with a best-fit f_{scatt} of 100%.

A final possibility may be ascribed to interactions between the jet and the putative torus. If the jet is beamed in a direction not along the line of sight, then the global matter distribution intercepts a larger fraction of the

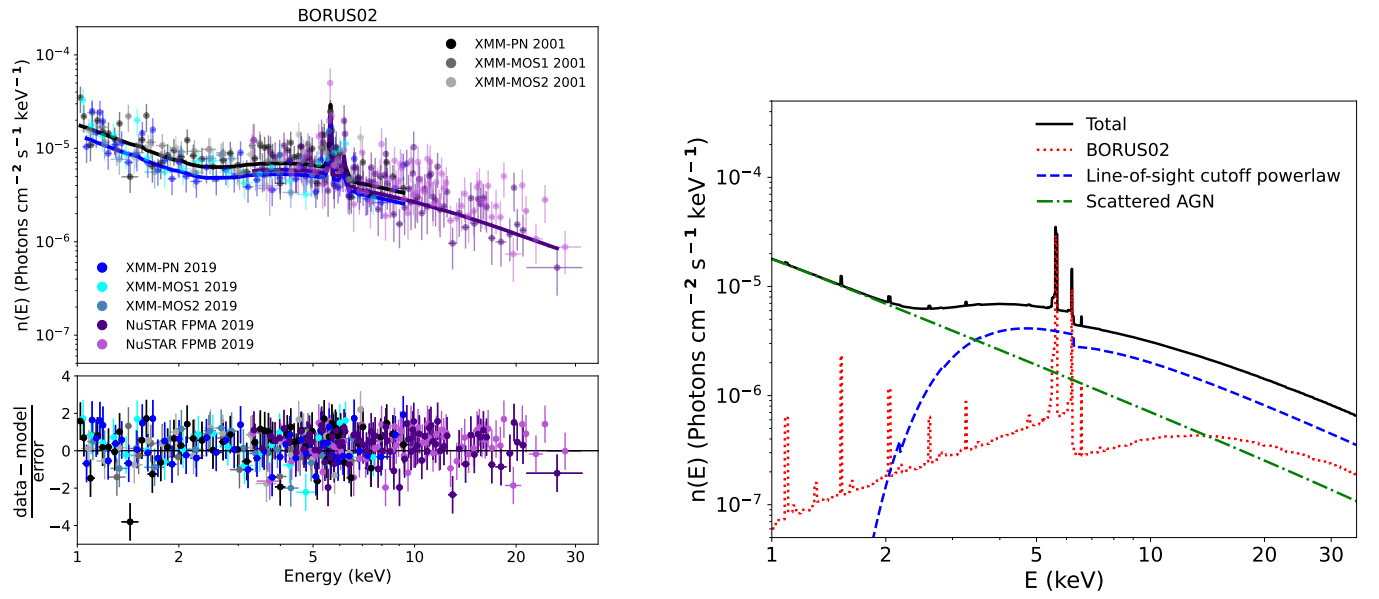


Figure 2. *Left:* The unfolded *XMM-Newton* and *NuSTAR* spectra fitted with the BORUS02 model, which has a lower energy cutoff of 1 keV that is higher than that of MYTORUS. *Right:* Best-fit model with individual model components plotted separately. According to this model, the spectrum is transmission dominated above 3 keV, with scattered AGN light being the main contributor to the X-ray spectrum at lower energies (compared with the MYTORUS model fits shown in Figure 1 where the scattered AGN component becomes dominant at energies below 2 keV).

intrinsic AGN energy (Figure 3, bottom), boosting the production of Fe K α line photons compared with those created along the line of sight (see Yaqoob et al. 1993, 1999). This intrinsic anisotropy will cause the transmitted continuum to appear to be suppressed relative to the global medium producing the bulk of the Fe K α emission, manifesting in the large Fe K α EW visible in the X-ray spectrum. Thus the relative normalization between the Compton scattered/fluorescent line component and transmitted component will be constrained to values greater than unity. Examples of radio jet interactions with the AGN obscuring medium have been previously observed: in-depth investigations of compact symmetric objects (radio loud AGN whose radio emission is contained within 1 kpc of the nucleus) reveal that the most compact of these radio objects reside in AGN with high column densities ($N_H > 10^{23} \text{ cm}^{-2}$), which suggests that higher density gas can restrict the expansion or production of larger scale radio jets (Sobolewska et al. 2019).

4.2. Consistency between X-ray and Mid-Infrared Emission

The dusty torus beyond the accretion disk and corona absorbs optical-ultraviolet photons and re-radiates this emission at mid-infrared (MIR) wavelengths. Coupling between the accretion disk and X-ray emitting corona would then impose a correlation between the mid-infrared and X-ray emission, which has been observed in a number of studies (Lutz et al. 2004; Ramos Almeida et al. 2007; Horst et al. 2008; Gandhi et al. 2009; Levenson et al. 2009; Hönig et al. 2010; Stern 2015). Taken a step further, observed X-ray emission that is heavily suppressed relative to the MIR emission is sometimes used as a proxy of Compton thick obscuration (Daddi et al. 2007; LaMassa et al. 2009, 2011; Bauer et al. 2010; Donley et al. 2012), though the X-ray to mid-infrared ratio can be influenced more by the spectral shape of the X-ray continuum and covering factor of the torus than the column density (Yaqoob & Murphy 2011).

Using the observed $12\mu\text{m}$ flux of 3C 223 from the *W3* magnitude of the All-*WISE* survey (Wright et al. 2010; Cutri et al. 2021), where *W3* = 7.8 (Vega), we can use the MIR-X-ray relation from Asmus et al. (2015) to estimate the intrinsic 2–10 keV luminosity. We find a predicted X-ray luminosity of $1.61 \times 10^{44} \text{ erg s}^{-1}$, which is about twice the value we derived from fitting the X-ray spectra with the MYTORUS scattered AGN model ($L_{2-10\text{keV}, \text{intrinsic}} = 7.4 \times 10^{43} \text{ erg s}^{-1}$). We note that this $L_{12\mu\text{m}} - L_{2-10\text{keV}}$ relation is derived using high-resolution MIR measurements that isolate the galaxy

cores, minimizing contamination from host galaxy star formation. The lower resolution *WISE* measurement encompasses the whole galaxy, which could be partially responsible for the higher predicted X-ray luminosity compared with our X-ray spectral measurements. Still, the agreement between the two values is within the scatter of the Asmus et al. (2015) relation ($\sigma \sim 0.3 \text{ dex}$), which is consistent with a physical link between the powering of the corona and heating of the torus.

4.3. Bolometric Output and Accretion Rate of the 3C 223 Black Hole

The Eddington luminosity ($L_{\text{Edd}} = 1.26 \times 10^{38} (M_{\text{BH}}/M_{\odot}) \text{ erg s}^{-1}$) represents the limit at which matter can accrete onto the central supermassive black hole. The Eddington ratio, defined as the ratio of the bolometric AGN luminosity (L_{bol}) to the Eddington luminosity ($\lambda_{\text{Edd}} = L_{\text{bol}}/L_{\text{Edd}}$), parameterizes the black hole accretion rate.

Since the line of sight to the accretion disk is obscured in Type 2 AGN, we are unable to calculate the black hole mass using virial mass estimators that relate the width of broad emission lines to the accretion disk luminosity. We thus use the empirical correlation between the black hole mass and velocity dispersion of stars in the host galaxy (i.e., $M_{\text{BH}}-\sigma$; Ferrarese & Merritt 2000) to estimate M_{BH} for the AGN in 3C 223. From a measured velocity dispersion of $\sigma = 202 \text{ km s}^{-1}$ (Bettoni et al. 2001), Woo & Urry (2002) used the Tremaine et al. (2002) $M_{\text{BH}}-\sigma$ relation to calculate a black hole mass of $\text{Log}(M_{\text{BH}}/M_{\odot}) = 8.15 \text{ dex}$ for 3C 223. L_{Edd} is thus $1.78 \times 10^{46} \text{ erg s}^{-1}$.

The AGN bolometric luminosity can be measured by integrating the AGN-only contribution to the multi-wavelength spectral energy distribution (SED). This procedure requires panchromatic coverage from rest-frame ultraviolet through mid-to-far infrared emission, and faces challenges from accurately decomposing host-galaxy from AGN emission (especially in Type 2 AGN). Alternate methods of estimating the bolometric luminosity involve measuring a quantity that traces the intrinsic AGN emission and applying a correction to extrapolate to the total AGN luminosity. We have two such intrinsic AGN indicators at our disposal: the optical [O III] line and the absorption-corrected 2–10 keV luminosity ($L_{2-10\text{keV}, \text{intrinsic}}$). We use both indicators and two different bolometric corrections to $L_{2-10\text{keV}, \text{intrinsic}}$ to estimate a range of possible Eddington ratios for 3C 223 that we report in Table 4.

[O III] forms in the AGN narrow line region (NLR), hundreds of parsecs beyond the obscuring torus, and is primarily ionized by accretion disk photons, making it

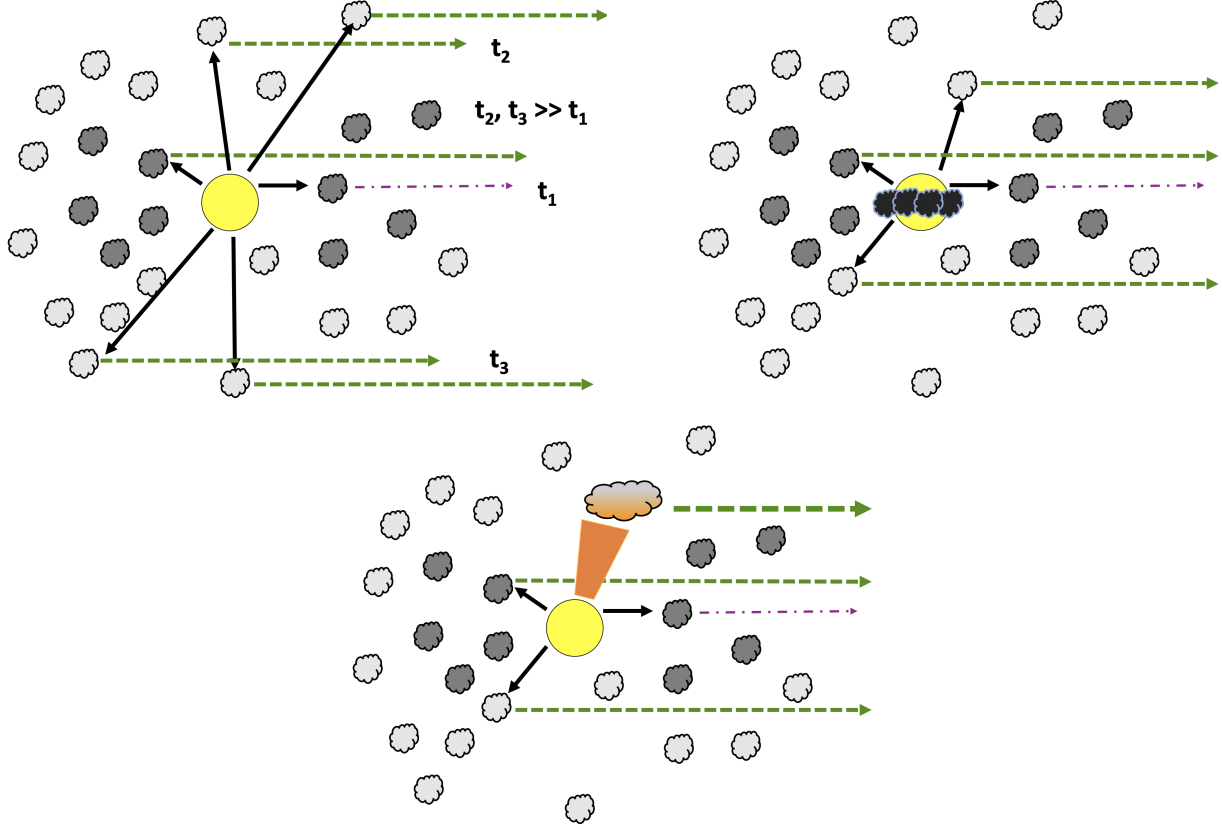


Figure 3. Illustrations of possible geometries that could give rise to an elevated A_s or f_{scatt} value. In all cases, the yellow circle marks the X-ray emitting source, the dark grey clouds represent high column density gas clouds ($> 10^{23} \text{ cm}^{-2}$), the light grey clouds indicate lower column density gas clouds (several $\times 10^{22} \text{ cm}^{-2}$), and the observer is on the right side of the panel. The black solid arrows represent direct emission from the X-ray source, the dash-dotted purple line denotes the zeroth-order continuum after being absorbed by the line-of-sight gas, and the green dashed lines illustrate the X-rays that have been Compton-scattered by the global distribution of clouds, producing the Fe $K\alpha$ line emission and continuum features of X-ray reprocessing. *Top left:* Here the Compton-scattering region lies many parsecs away from the X-ray source while the line-of-sight clouds are much closer in, such that the time delay between observing the Compton-scattered photons (t_2, t_3) and absorbed line-of-sight photons (t_1) is much greater than the time period of the observations. *Top right:* In this scenario, the X-ray emitting region is obscured by a patchy equatorial ring of heavily Compton-thick material ($N_H > 10^{26} \text{ cm}^{-2}$, black clouds in diagram), allowing only a fraction of light to intercept the lower column density line-of-sight clouds while the global distribution of matter has a largely unimpeded view of the X-ray source. *Bottom:* A jet beamed in a direction not along the line of sight (shown in orange), can impart significant energy to the cloud that it illuminates (orange colored cloud), boosting the production of Fe $K\alpha$ photons (thicker green dashed line) compared with those generated in the line-of-sight obscuring clouds.

a reasonable proxy of the intrinsic AGN emission (e.g., Mulchaey et al. 1994; Kauffmann et al. 2003; LaMassa et al. 2010). Liu et al. (2009) calibrated the bolometric correction to $L_{[\text{O III}]}$ for Type 2 quasars from SDSS using:

$$\text{Log} \left(\frac{L_{\text{bol}}}{L_{\odot}} \right) = 0.99 \times \text{Log} \left(\frac{L_{[\text{O III}]}}{L_{\odot}} \right) + 3.5. \quad (1)$$

They quote an uncertainty of 0.5 dex in L_{bol} for this relation. We note that one factor that can contribute to this uncertainty is reddening towards the narrow line region which can attenuate the observed [O III] emission (see, e.g., Lamstra et al. 2009). On the other hand, local ionization from jet heating can power the optical emitting line region (Holt et al. 2008; Nesvadba et al. 2008), meaning that the [O III] line may not cleanly trace AGN ionization in radio loud sources (see, e.g., 4C+29.30; van Breugel et al. 1986; Siemiginowska et al. 2012; Couto et al. 2020). With these caveats in mind, the observed $\text{Log}(L_{[\text{O III}]} / L_{\odot})$ value of 8.78 dex (Reyes et al. 2008) indicates an [O III]-determined bolometric AGN luminosity of $L_{\text{bol},[\text{O III}]} = 5.93 \times 10^{45} \text{ erg s}^{-1}$, for an Eddington ratio of $\lambda_{\text{Edd},[\text{O III}]} = 0.33$.

The form of the X-ray bolometric correction likely depends on bolometric AGN luminosity (Marconi et al. 2004; Hopkins et al. 2007) or Eddington ratio (Vasudevan & Fabian 2007; Lusso et al. 2010). Using the relations for the bolometric correction calibrated on Type 2 AGN from the *XMM-COSMOS* survey from Lusso et al. (2012), we estimate L_{bol} and λ_{Edd} from our measured intrinsic 2-10 keV X-ray luminosity derived via the MYTORUS scattered AGN model ($L_{2-10\text{keV},\text{intrinsic}} = 7.4 \times 10^{43} \text{ erg s}^{-1}$, Table 2). We calculate these parameters using both the calibrated L_{bol} -dependent and λ_{Edd} -dependent bolometric correction relations presented in Lusso et al. (2012).

The functional form of the L_{bol} -dependent bolometric correction is:

$$\text{Log} \left(\frac{L_{\text{bol}}}{L_{2-10\text{keV}}} \right) = 0.23x + 0.05x^2 + 0.001x^3 + 1.256, \quad (2)$$

where $x = \text{Log}(L_{\text{bol}} / L_{\odot}) - 12$. We solved for L_{bol} numerically given our intrinsic X-ray luminosity measurement, finding $L_{\text{bol},2-10\text{keV}} = 1.0 \times 10^{45} \text{ erg s}^{-1}$ with $\lambda_{\text{Edd},2-10\text{keV}} = 0.06$.

The calibrated λ_{Edd} -dependant bolometric correction for Type 2 AGN is given by:

$$\text{Log} \left(\frac{L_{\text{bol}}}{L_{2-10\text{keV}}} \right) = 0.621x + 1.947, \quad (3)$$

where $x = \text{Log}(\lambda_{\text{Edd}})$ (Lusso et al. 2012). This relation gives $\lambda_{\text{Edd}} = 0.07$ and a bolometric luminosity of $1.3 \times 10^{45} \text{ erg s}^{-1}$.

Taken together, and given the uncertainties in the relationships and the measured values, we conclude that the AGN in 3C 223 is accreting at greater than 5% Eddington. This accretion rate is consistent with that of other high excitation radio galaxies (HERG), pointing to radiatively efficient accretion described by the standard Shakura & Sunyaev (1973) optically thick, geometrically thin accretion disk model (Best & Heckman 2012). We note that Hardcastle et al. (2007) proposed that major galaxy mergers can provide a reservoir of cold gas for powering radiatively efficient accretion in HERGs, but *Hubble Space Telescope* images of 3C 223 do not reveal morphological evidence of recent merger activity (Madrid et al. 2006).

4.4. Radio Properties

Typical of FR II radio galaxies, VLA images of 3C 223 at 20 cm and 8.4 GHz depict a radio core at the center of the AGN with extended radio lobes that span about 1.5-2 arcminutes to the Northwest and Southeast directions (Baum et al. 1988; Massaro et al. 2012). The radio lobes extend in declination from approximately $35:51:30 < \delta < 35:53:00$ and $35:54:45 < \delta < 35:56:30$ (J2000 coordinates). We extracted the X-ray spectra from a circular aperture centered at the X-ray centroid of the AGN core ($\alpha = 9:29:52.95$, $\delta = 35:53:58.5$) with a $30''$ radius aperture for *XMM-Newton* and a $45''$ radius aperture for *NuSTAR*. The X-ray emission we analyzed is spatially coincident with the radio core but does not have contributions from the extended lobes. As noted previously, we took care to sample the background from a region that did not overlap with the radio lobes.

We compare the amount of energy released by the radio jet in the core of the galaxy with the AGN radiative power estimated in the previous section. The jet kinetic power can be quantified using $P_{\text{mech,cavity}} = 3 \times 10^{37} (L_{1.4\text{GHz}} / 10^{25} \text{ W})^{0.68} \text{ W}$ (Heckman & Best 2014). 3C 223 has a measured 1.4 GHz flux density of 3.54 Jy (Kuźmicz et al. 2018), which gives a jet luminosity of $2.1 \times 10^{45} \text{ erg s}^{-1}$. This value is 12% of our calculated Eddington luminosity, exceeding the intrinsic X-ray luminosity we measured, and is comparable to our estimates of the radiative bolometric luminosity.

4.5. 3C 223 in Type 2 Quasar Parameter Space

The incidence of Compton-thick obscured quasars, the most luminous AGN, is of particular interest since some studies show a clear decline in AGN obscuration as luminosity increases (the ‘‘receding torus’’ model, Lawrence & Elvis 1982; Ueda et al. 2003; Merloni et al. 2014; Brightman et al. 2014), though this could be due to the difficulty in finding the most heavily obscured AGN

Table 4. 3C 223 AGN Physical Parameters^a

Parameter	Value	Reference
$\text{Log}(M_{\text{BH}}/M_{\odot})$	8.15 dex	Woo & Urry (2002)
L_{Edd} (erg s ⁻¹)	1.78×10^{46}	...
$L_{[\text{O III}]}$ (erg s ⁻¹)	2.29×10^{42}	Reyes et al. (2008)
$L_{[\text{O III}],\text{intrinsic}}$ (erg s ⁻¹) ^b	5.81×10^{42}	...
$L_{\text{bol},[\text{O III}]}$ (erg s ⁻¹) ^c	5.93×10^{45}	Liu et al. (2009)
$\lambda_{\text{Edd},[\text{O III}]}$	0.33	...
$L_{\text{bol},2-10\text{keV}}^{\text{d}}$	1.0×10^{45}	Lusso et al. (2012)
$\lambda_{\text{Edd},2-10\text{keV}}^{\text{d}}$	0.06	...
$L_{\text{bol},2-10\text{keV}}^{\text{e}}$	1.3×10^{45}	Lusso et al. (2012)
$\lambda_{\text{Edd},2-10\text{keV}}^{\text{e}}$	0.07	...
L_{jet} (erg s ⁻¹) ^f	2.1×10^{45}	...

^aWe estimated the AGN bolometric luminosity (L_{bol}) and Eddington ratio (λ_{Edd}) using the [O III] emission line and intrinsic 2-10 keV luminosity. The reported subscripts on these parameters refer to the quantity used to derive L_{bol} and λ_{Edd} . For L_{bol} and λ_{Edd} derived from $L_{2-10\text{keV},\text{intrinsic}}$, we used two different functional forms of the bolometric correction.

^bExtinction-corrected [O III] luminosity. See Section 4.5 and Appendix D for details.

^c $L_{[\text{O III}]}$ measured from Reyes et al. (2008) and bolometric correction to $L_{[\text{O III}]}$ from Liu et al. (2009). Note that jet heating could contribute to the [O III] line luminosity in radio loud AGN (e.g., van Breugel et al. 1986; Couto et al. 2020).

^dUsing the L_{bol} -dependent bolometric correction relation for Type 2 AGN from Lusso et al. (2012) and $L_{2-10\text{keV},\text{intr}} = 7.4 \times 10^{43}$ erg s⁻¹ from the MYTORUS scattered AGN model.

^eUsing the λ_{Edd} -dependent bolometric correction relation for Type 2 AGN from Lusso et al. (2012) and $L_{2-10\text{keV},\text{intr}} = 7.4 \times 10^{43}$ erg s⁻¹ from the MYTORUS scattered AGN model.

^fJet luminosity using $P_{\text{mech,cavity}} = 3 \times 10^{37} (L_{1.4\text{GHz}}/10^{25}\text{WHz}^{-1})^{0.68}$ W (Heckman & Best 2014), and $L_{1.4\text{GHz}} = 3.54$ Jy (Kuzmicz et al. 2018)

(e.g., Mateos et al. 2017), and if there is a physical connection, the accretion rate rather than the AGN luminosity may be the driver (Winter et al. 2009; Ricci et al. 2017). Certainly a better census of the obscuration levels in the most luminous AGN would shed light on whether the apparent receding torus phenomenon is an observational bias or a physical effect, and if the latter, the roles that accretion rate and AGN energy output may play in shaping the circumnuclear environment.

Significant efforts have been made to reliably identify Type 2 quasars and then assess their obscuring column densities to identify the Compton-thick population. One

method for identifying Compton-thick AGN relies on selecting obscured AGN on the basis of intrinsic AGN luminosity proxies that are relatively unaffected by the amount of circumnuclear obscuration and then examining the X-ray properties of these sources to search for evidence of Compton-thick obscuration (Bassani et al. 1999; Heckman et al. 2005; Panessa et al. 2006; LaMassa et al. 2009, 2011, 2014; Jia et al. 2013). As noted above, the [O III] line is one commonly used proxy of intrinsic AGN emission used to select samples of obscured AGN.

Reyes et al. (2008) selected a sample of Type 2 quasars from SDSS that have optical emission line ratios consistent with AGN photionization and [O III] luminosities exceeding $L_{[\text{O III}]} > 10^{8.3} L_{\odot}$ (7.64×10^{41} erg s⁻¹; Zakamska et al. 2003). 3C 223 (designated as SDSS J093952.74+355358.0) was included in this sample and was subsequently analyzed by Jia et al. (2013) as part of an effort to analyze the X-ray spectra of [O III]-selected Type 2 quasars to estimate the Compton-thick fraction.

Nine other [O III]-selected Type 2 quasar candidates have been observed by *NuSTAR* from the Reyes et al. (2008) and Jia et al. (2013) sample (see also Vignali et al. 2006, 2010): Mrk 34 ($z = 0.051$; Gandhi et al. 2014) and eight additional sources reported in Lansbury et al. (2014) and Lansbury et al. (2015) that lie in the redshift range between $0.094 < z < 0.49$. Of these nine, only Mrk 34 and one quasar from Lansbury et al. (2015) (SDSS J121839.40+470627.7, $z = 0.094$) were detected with adequate numbers of counts with *NuSTAR* to permit spectral fitting with the MYTORUS model. Both are confirmed to be Compton-thick based on measuring their column densities and have intrinsic 2-10 keV X-ray luminosities computed. Lansbury et al. (2014, 2015) infer heavy obscuration in the remaining [O III]-selected Type 2 quasars by comparing $L_{2-10\text{keV}}/L_{6\mu\text{m}}$ and $L_{10-40\text{keV}}/L_{6\mu\text{m}}$ to the X-ray - mid-infrared relation found for local AGN (Lutz et al. 2004).⁴

To the list of SDSS [O III]-selected Type 2 quasars, we include Type 2 AGN from the 70-month Swift-BAT hard X-ray (> 10 keV) survey (Baumgartner et al. 2013) whose [O III] luminosities exceed the $L_{[\text{O III}]} > 10^{8.3} L_{\odot}$ quasar threshold defined in Zakamska et al. (2003) and applied in Reyes et al. (2008). Like all X-ray surveys, the Swift-BAT survey has lower sensitivity to AGN that are Compton-thick along the line of sight (e.g., LaMassa et al. 2010), but our goal here is to augment the comparison sample of Type 2 quasars observed with *NuSTAR*. As *NuSTAR* has been conducting a legacy survey of *Swift*

⁴ $L_{6\mu\text{m}}$ refers to the rest-frame, reddening-corrected 6 μm luminosity.

BAT sources since 2012 (Alexander et al. 2013), this dataset provides us a larger baseline for comparison.

Using emission line flux measurements from the BAT AGN Spectroscopic Survey (BASS; Koss et al. 2017), we identified 21 Type 2 AGN that can be classified as quasars on the basis of their [O III] luminosity. Of these, three were observed by *NuSTAR* and their broad-band X-ray spectrum (0.5 - 80 keV) fitted with MYTORUS by Marchesi et al. (2018): MCG +08-03-018 ($z = 0.021$), CGCG 420-015 ($z = 0.030$), and NGC 3393 ($z = 0.013$). Marchesi et al. (2019) measure a Compton-thick line-of-sight column density for NGC 3393, and heavily obscured, but Compton-thin column densities for the other two AGN ($\sim 5 - 8 \times 10^{23} \text{ cm}^{-2}$, but see Marchesi et al. 2019, for measured Compton-thick N_{H} values when using the BORUS2 X-ray spectral model (Baloković et al. 2018) with a free covering factor). From these fits, Marchesi et al. (2018) calculated absorption-corrected 2-10 keV luminosities that we use below.

In Figure 4, we compare the [O III] and 2-10 keV luminosity of these quasars with the Panessa et al. (2006) $L_{2-10\text{keV}}$ vs. $L_{[\text{O III}]}$ relation for Type 1 Seyferts and quasars: $\text{Log}(L_{2-10\text{keV}}) = (0.95 \pm 0.07)L_{[\text{O III}]} + (3.87 \pm 2.76)$. Their Sy1 sample was selected from the Ho et al. (1997) catalog and supplemented with quasars from Mulchaey et al. (1994) and Alonso-Herrero et al. (1997). For this analysis, Panessa et al. (2006) used [O III] fluxes reported in Ho et al. (1997) that were corrected for reddening within the NLR. We followed this prescription to estimate the intrinsic [O III] luminosity ($L_{[\text{O III}],\text{intrinsic}}$) using the observed Balmer decrement (i.e., $H\alpha/H\beta$) normalized by an intrinsic value of 3.1 (see Osterbrock & Ferland 2006) and the extinction law of Cardelli et al. (1989):

$$L_{[\text{O III}],\text{intrinsic}} = L_{[\text{O III}],\text{observed}} \left(\frac{L_{H\alpha}/L_{H\beta}}{3.1} \right)^{3.2}, \quad (4)$$

(see Appendix D for the derivation). With an observed Balmer decrement of 4.15, $L_{[\text{O III}],\text{intrinsic}} = 5.81 \times 10^{42} \text{ erg s}^{-1}$ for 3C 223. Due to the high redshift of some of the Type 2 SDSS-selected quasars in the Lansbury et al. (2014, 2015) samples, $H\alpha$ does not fall within the observed optical spectrum, so the [O III] luminosities for these sources are lower limits in Figure 4. For all three BASS Type 2 quasars, the observed Balmer decrement was lower than the assumed intrinsic value, so no reddening correction was applied.

Figure 4 shows that nearly all the Type 2 quasars considered here have X-ray luminosities below the $L_{2-10\text{keV}} - L_{[\text{O III}]}$ relation from Panessa et al. (2006). Though there is a wide spread on the best-fit values for this relation, the suppressed X-ray emission indi-

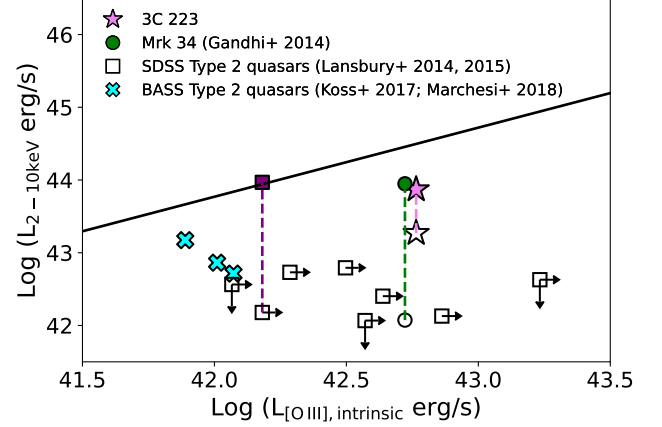


Figure 4. X-ray luminosity (2-10 keV) as a function of [O III] luminosity for 3C 223 and other [O III]-selected Type 2 quasars observed by *NuSTAR*. Filled data points represent the absorption-corrected 2-10 keV luminosity (using the MYTORUS scattered AGN model for 3C 223) and unfilled data points denote the observed 2-10 keV luminosity. The $L_{2-10\text{keV}} - L_{[\text{O III}],\text{intrinsic}}$ relation for Type 1 AGN from Panessa et al. (2006) is overplotted. Though there is a wide spread in the Panessa et al. (2006) relation, most Type 2 quasars have intrinsic X-ray luminosities systematically below the Type 1 relation. Type 2 quasars may be inherently weaker in X-rays, even when accounting for absorption, than their Type 1 counterparts.

cates that even after correcting for absorption, Type 2 quasars are more X-ray weak than their Type 1 counterparts.

4.6. The Dearth of Compton-Thick Radio Loud AGN?

Ursini et al. (2018) posed an interesting question: whether Compton-thick radio loud AGN? They claimed that when obtaining high quality hard X-ray spectra ($>10 \text{ keV}$) of Compton-thick radio loud AGN candidates, there has yet to be unequivocal evidence of column densities exceeding $1.25 \times 10^{24} \text{ cm}^{-2}$ measured from models that accurately treat the effects of Compton scattering (e.g., MYTORUS, Murphy & Yaqoob 2009; SPHERE and TORUS, Brightman & Nandra 2011; BORUS02, Baloković et al. 2018). They analyzed archival *NuSTAR* spectra of three radio loud, Type 2 heavily absorbed AGN candidates from Panessa et al. (2016) using MYTORUS in the default “coupled” configuration, freezing the inclination angle at 90° (NGC 612, 4C 73.08, 3C 452). The fitted equatorial column densities range from $\sim 4 - 9 \times 10^{23} \text{ cm}^{-2}$.

To date, there have been two other radio loud, Type 2 AGN observed by *NuSTAR* and modeled with MYTORUS that allow for a direct comparison with our re-

sults. Centaurus A has a fitted equatorial column density of $1.10^{+0.15}_{-0.02} \times 10^{23} \text{ cm}^{-2}$ for an inclination angle $\geq 76^\circ$ (Fürst et al. 2016), which is consistent with its line-of-sight column density of $\sim 1.1 \times 10^{23} \text{ cm}^{-2}$ measured from *Suzaku* observations (Tzanavaris et al. 2021). Cygnus A, whose X-ray spectra includes contributions from the intracluster medium in which it is embedded and shows signatures of a fast, highly ionized outflow, is obscured by a line-of-sight column density of $\sim 1.6 \times 10^{23} \text{ cm}^{-2}$. However, when Reynolds et al. (2015) fit the X-ray spectra with MYTORUS in decoupled mode, they find an average global column density that is Compton-thick ($N_{\text{H,global}} = 1.9^{+1.0}_{-0.8} \times 10^{24} \text{ cm}^{-2}$).

We find a comparable column density for 3C 223 to those reported in the literature for other Type 2, radio loud AGN observed with *NuSTAR* ($1 - 9 \times 10^{23} \text{ cm}^{-2}$): heavily obscured, but not Compton-thick.⁵ Whether this heavy obscuration is along the line of sight or represents the global average column density depends on the spectral model.

Interestingly, clear cases of globally Compton-thick radio loud AGN comes from two Type 1 (broad line) AGN: Mrk 668 (Sobolewska et al. 2019) and 4C 74.26 (Tzanavaris et al. 2019). Mrk 668, a Gigahertz Peaked-Spectrum source, was first suggested to be Compton-thick based on features of reprocessing in its *XMM-Newton* spectrum (Guainazzi et al. 2004). Follow-up observations with *NuSTAR* and modeling of the *Chandra* plus *NuSTAR* spectra with the MYTORUS and Baloković et al. (2018) TORUS model demonstrated that the torus is patchy with a global column density that is Compton-thick and about four times higher than the (Compton-thin) line-of-sight column density (Sobolewska et al. 2019). Similarly, the *Suzaku* and *NuSTAR* spectra of 4C 74.26 were fitted with MYTORUS to reveal a patchy obscuring medium that is Compton-thick globally while Compton-thin along the line of sight (Tzanavaris et al. 2019).

Radio loud AGN enveloped in Compton-thick levels of obscuring gas do exist. Contrary to expectations from simple one-dimensional models, this Compton-thick material is not observed along the line of sight but is present in the global average column density, and imprints signatures of Compton scattering on the observed X-ray spectrum. Currently, there are three known examples of

globally Compton-thick radio loud AGN, one of which is optically obscured (Cygnus A) and two of which are optically unobscured (Mrk 668 and 4C 74.26). Additionally, there are instances of heavily obscured radio loud AGN that have complex environments that are best fit by absorption models requiring distinct column densities (e.g., 4C+29.30, Sobolewska et al. 2012). More high-energy X-ray observations above 10 keV are needed to test whether the fraction of radio loud AGN with Compton-thick reprocessing gas is systematically lower than radio quiet AGN, and whether such a trend, if it does exist, implicates evolutionary or environmental origins.

5. CONCLUSIONS

We analyzed the *XMM-Newton* and *NuSTAR* spectra of 3C 223, a radio loud Type 2 quasar using the physically-motivated, self-consistent BORUS02 model (Baloković et al. 2018) and MYTORUS model (Murphy & Yaqoob 2009), testing both a scattered AGN origin (“MYTORUS scattered AGN”) and jet origin (“MYTORUS jet”) for the soft emission. We find that the broad band X-ray spectra (0.5 - 30 keV) are best described by a model where the X-ray reprocessing material is patchy, consisting of gas clouds with a high, though not Compton-thick, column density ($N_{\text{H}} > 10^{23} \text{ cm}^{-2}$), and gas clouds with much lower column densities (several $\times 10^{22} \text{ cm}^{-2}$). The spectral models give conflicting results about whether the high column density gas is distributed along the line of sight (MYTORUS scattered AGN model), or represents the global average column density (MYTORUS jet model and BORUS02 model; Tables 2-3). The inhomogeneous nature of the X-ray obscuring medium confirms the results presented in LaMassa et al. (2014) from analysis of the *XMM-Newton* data only. Though all three models provide good fits to the spectra of similar statistical significance, the latter two models find a best-fit AGN spectral slope at the lower limit allowed by the models ($\Gamma_{\text{limit}} = 1.4$), while the spectral slope from the MYTORUS scattered AGN model is consistent with typical AGN values ($\Gamma = 1.91^{+0.33}_{-0.27}$; Reeves & Turner 2000). The BORUS02 model fit gives an elevated iron abundance that is about twice that of the solar value.

We find a relatively high normalization between between the transmitted continuum and the Compton scattered emission ($A_{\text{s}} \sim 5 - 6$) for the MYTORUS models and an unphysically high scattering fraction ($f_{\text{scatt}} \sim 27\%$) for the BORUS02 model, even when allowing the iron abundance to be a free parameter in the spectral fitting. These fitted parameters indicate that additional physics beyond those accounted for in the

⁵ For MYTORUS inclination angles of 90° , the equatorial column density ($N_{\text{H,equatorial}}$) from the “coupled” configuration is equivalent to the line-of-sight column density ($N_{\text{H,los}}$) in our “decoupled” configuration. Thus our $N_{\text{H,los}}$ measurement can be directly compared to the equatorial N_{H} values for NGC 612, 4C 73.08, and 3C 452 reported in Ursini et al. (2018).

MYTORUS and BORUS02 calculations are shaping the emergent spectrum, namely the strength of the Fe K α line compared with the continuum. Some possibilities, illustrated in Figure 3, include:

- *Variability*: Since no variability was observed in the 18 year window between *XMM-Newton* epochs (Appendix A), this scenario would require the Compton-scattering region to extend beyond 5.5 pc (i.e., the 18 year light-travel time between *XMM-Newton* observations). Detailed studies of local AGN demonstrate that most of the Fe K α line emission originates on nuclear scales (e.g., Gandhi et al. 2014), but there is an extended Compton-scattering region beyond the several-parsec torus (Bauer et al. 2015; Fabbiano et al. 2017, 2018; Jones et al. 2020; Yi et al. 2021).
- *Inner Compton-thick ring*: A ring of heavily Compton-thick material with a column density exceeding 10^{26} cm^{-2} could completely block $\sim 80\%$ of the light in the equatorial direction, causing the global distribution of clouds to see about five - six times more radiation than clouds along the line of sight. We note that modeling the spectra with UXCLUMPY (Buchner et al. 2019) to test for the presence of a $N_{\text{H}} > 10^{25} \text{ cm}^{-2}$ ring did not provide an acceptable fit (Appendix C).
- *Interaction of jet with the torus*: The jet may be imparting a great deal of energy beamed in a direction not along the line of sight, enhancing Fe K α emission in the global medium relative to the line of sight.

With future *ATHENA* X-ray Integral Field Unit observations (Barret et al. 2018), which will have $\sim 5''$ pixels and a spectral resolution of 2.5 eV, we could test how much of the Fe K α emission originates from extended scales ($5'' \sim 10 \text{ kpc}$ for 3C 223) and whether it is aligned with the more distant radio and X-ray lobes which would help distinguish between the scenarios above.

From the intrinsic (absorption-corrected) X-ray luminosity and [O III] luminosity, we estimate a radiative bolometric luminosity of $\sim 1 - 6 \times 10^{45} \text{ erg s}^{-1}$ and an Eddington ratio of $\gtrsim 5\%$, consistent with radiatively efficient accretion (Section 4.3). The bolometric luminosity, and associated Eddington ratio, calculated from the [O III] line is greater than that calculated from the X-ray luminosity, but it is unclear whether this result is due to the radio jet boosting the [O III] line luminosity (van Breugel et al. 1986; Siemiginowska et al. 2012; Couto et al. 2020) or whether an inner, heavily Compton-thick ring of obscuration is causing the intrinsic X-ray lumi-

nosity deduced by the MYTORUS model to be under-predicted. The amount of kinetic energy carried by the jet ($2.1 \times 10^{45} \text{ erg s}^{-1}$) is comparable to that of the radiatively bolometric luminosity (Section 4.4). 3C 223 and other Type 2 [O III]-defined quasars observed by *NuSTAR* generally have suppressed X-ray emission compared with Type 1 AGN studied by Panessa et al. (2006, Figure 4), suggesting that Type 2 quasars may be inherently weaker in X-rays than their Type 1 counterparts.

Finally, we return to the question of whether there is a dearth of radio loud Compton-thick AGN. From reviewing the literature, we found three radio loud AGN observed by *NuSTAR* whose X-ray spectra are well fit by models that measure a Compton-thick global average column density, yet Compton-thin line-of-sight column density: Type 2 (optically obscured) AGN Cygnus A (Reynolds et al. 2015) and Type 1 (optically *unobscured*) AGN Mrk 668 (Sobolewska et al. 2019) and 4C 74.26 (Tzanavaris et al. 2019). Current evidence demonstrates that globally Compton-thick radio loud AGN do exist. However, these confirmed cases have complicated spectra that require physically motivated models to disentangle the global from the line-of-sight column density. The presence of Compton-thick gas in these sources could be missed by simpler one dimensional models or those that assume a homogeneous obscuring medium. As the number of detailed broadband X-ray spectroscopic studies of individual AGN increases (LaMassa et al. 2014; Yaqoob et al. 2015; Baloković et al. 2018; Reynolds et al. 2015; Sobolewska et al. 2019; Tzanavaris et al. 2021), so too does the census of those that have demonstrable evidence that the X-ray reprocessor is non-uniform, supporting an emerging picture that the gaseous environment that reprocesses emission around an accreting black hole can be complex and that binary characterizations of Compton-thin and Compton-thick oversimplifies reality.

We thank the anonymous referee for a careful reading of this manuscript and thoughtful comments which improved the quality of the paper. S.M.L acknowledges support from NASA grants 80NSSC20K0261 and 80NSSC20K0837. S.M.L is thankful for the efforts of STScI IT, facilities, and administrative staff that allowed continual operations at STScI, even during difficult conditions in the early stages of the COVID-19 pandemic. This paper would not be possible without their support. A.S. was supported by NASA contract NAS8-03060 (Chandra X-ray Center).

Based on observations obtained with XMM-Newton, an ESA science mission with instruments and contributions directly funded by ESA Member States and NASA.

This research has made use of the NuSTAR Data Analysis Software (NuSTARDAS) jointly developed by the ASI Space Science Data Center (SSDC, Italy) and the California Institute of Technology (Caltech, USA). This research has made use of the NASA/IPAC Extragalactic Database (NED), which is funded by the National Aeronautics and Space Administration and operated by the California Institute of Technology. The scientific results reported in this article are based in part on data obtained from the Chandra Data Archive. This research has made use of software provided by the Chandra X-ray Center (CXC) in the application package CIAO. This research has made use of the NASA/IPAC Extragalactic Database (NED), which is funded by the National Aeronautics and Space Administration and operated by the California Institute of Technology.

Facilities: XMM,NuSTAR,CXO

Software: XSpec (v12.11.1; Arnaud 1996), NuSTAR-DAS (v2.0.0), CIAO (v4.13; Fruscione et al. 2006)

3C 223

APPENDIX

A. VARIABILITY

We investigated whether the X-ray spectrum of 3C 223 exhibits evidence of variability between the initial *XMM-Newton* observations from 2001 and the most recent observations from 2019. For this test, we included analysis of a short (8 ks) *Chandra* observation of 3C 223 taken in 2012 as part of a snapshot survey of 3C radio sources (PI: Harris, ObsID: 12731; [Massaro et al. 2012](#)). The *Chandra* data were processed with CIAO v. 4.13 and CALDB 4.9.5 ([Fruscione et al. 2006](#)). We ran the recommended CHANDRA_REPRO script to generate a calibrated events file from which we extract the *Chandra* spectrum of 3C 223, with the source spectra extracted from a $3''$ radius circle centered on the peak X-ray emission of the source, and the background derived from an annulus with an inner radius of $5''$ and $20''$. We note that in this short exposure, we see no evidence of the extended X-ray lobes reported in the *XMM-Newton* spectra by [Croston et al. \(2004\)](#) and expect that this region is dominated by X-ray background photons. The spectra were binned with Ftgrouppha, with a minimum S/N of 2 per bin in the background subtracted spectrum.

We fitted the two epochs of *XMM-Newton* spectra and the *Chandra* spectrum between 0.5-10 keV with a phenomenological double absorbed powerlaw model with a Gaussian component for modeling the Fe $K\alpha$ emission. A constant multiplicative factor was included in the modeling to serve as the cross-detector and cross-instrument normalization. Despite concerted cross-calibration efforts across missions, systematic differences up to 10-15% in the absolute flux calibration often remain (e.g., [Madsen et al. 2017](#)). The results of this spectral fitting are shown in Figure 5, where we show only the *XMM-Newton* PN spectra from 2001 and 2019 for clarity, though the MOS1 and MOS2 spectra for both epochs were included in the fitting.

The intrinsic spectrum shows no evidence of variability from 2001 to 2012 to 2019: none of the spectra show systematic deviations from the best-fit model. The overall normalization between spectral epochs show some differences. The average normalization of the *XMM-Newton* spectra from 2001 (2019) is 1.00 ± 0.18 (0.82 ± 0.17), with the *Chandra* normalization equal to $0.64^{+0.12}_{-0.11}$. These cross-calibration normalizations are consistent within the 90% confidence interval between the *XMM-Newton* spectra and between the *Chandra* spectrum and *XMM-Newton* spectra from 2019. The systematically lower normalization for the *Chandra* spectrum, though not statistically significant, could be due to unresolved emission at scales larger than the $3''$ radius circular aperture used for the *Chandra* spectrum that is observed in the deeper *XMM-Newton* data extracted from the larger $30''$ radius aperture.

B. RULING OUT OTHER MYTORUS MODEL FITS

When trying multiple MYTORUS configurations to fit the X-ray spectra of 3C 223, we modeled the soft X-ray emission (0.5 - 2 keV) as originating from scattered AGN light or from the base of a radio jet. We summarize the results in Table 5 and Table 6, ascribing the soft emission to scattered AGN flux or jet emission, respectively. In Figure 6, we show close ups around the Fe $K\alpha$ line for the scattered AGN model only since the plots for the jet model look identical, with the exception of the decoupled MYTORUS jet model with a frozen A_S value at unity, which shows a similar fit to Fe $K\alpha$ as the decoupled MYTORUS jet model where A_S is a free parameter. Nevertheless, we reject the former model description as allowing A_S to be a free parameter improves the fit at a significant level according to the F -test (F statistical value of 16.03 with a probability of 7.4×10^{-5} that the improvement is due to chance).

In the coupled MYTORUS realization, the torus is assumed to be azimuthally symmetric and homogeneous and the fitted column density represents the equatorial column density ($N_{\text{H,equatorial}}$). In these cases, the fitted inclination angle of the torus is constrained to be at the boundary of intersecting the line of sight ($\sim 60^\circ$). Such “grazing” inclination angles indicate that the model is reconciling the need for a high global column density to account for strong Fe $K\alpha$ emission relative to the continuum (i.e., high Fe $K\alpha$ EW) with an observed continuum shape that does not have the severe low-energy spectral curvature that would be associated with such high-to-Compton-thick column densities. Fitted grazing inclination angles are thus a clue that the X-ray reprocessor is not homogeneous.

We also explored MYTORUS model options where the relative normalization between the transmitted and Compton scattered components of the model (A_S) is frozen to unity and when it is allowed to be fitted as a free parameter. We found that when A_S is constrained to unity, both the Fe $K\alpha$ line and continuum around the Fe $K\alpha$ line is poorly fit (Figure 6, left panel), compared to our best fit model (Figure 6, bottom right panel). Though the coupled MYTORUS model fit with free A_S shows an acceptable fit around the Fe $K\alpha$ complex (Figure 6, upper right), this model can be ruled out due to the grazing inclination angle found for the torus that disfavors a homogenous obscuring medium as assumed by the default MYTORUS model set-up.

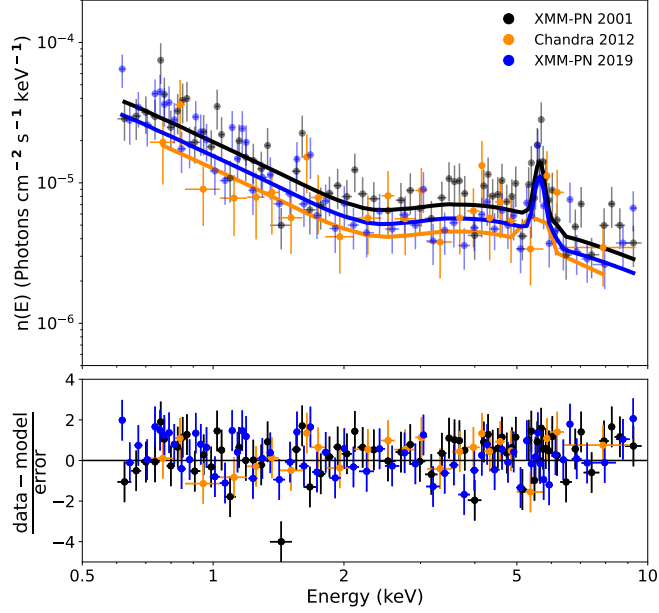


Figure 5. Results from fitting the *XMM-Newton* and *Chandra* spectra with a phenomenological double powerlaw + Gaussian model to search for indications of variability between epochs. No deviations in the observed spectra from the best-fit model are evident, indicating that the intrinsic X-ray spectrum has not varied significantly at the times of these observations. The overall normalization for the *Chandra* spectrum is lower than that of the *XMM-Newton* spectra, which could be instrumental or due to unresolved X-ray emission being captured in the deeper *XMM-Newton* observations. For clarity, only the spectra from the *XMM* PN detector are plotted, though we included the MOS1 and MOS2 spectra from both epochs when fitting the dataset.

C. FITTING UXCLUMPY TO 3C 223 X-RAY SPECTRA

The UXCLUMPY (Unified X-ray CLUMPY) model is based on a geometry where the X-ray reprocessor takes the form of discrete clouds that can have a range of column densities and angular distributions (Buchner et al. 2019). XSPEC table models are available that are derived from Monte Carlo simulations that use the XARS (X-ray Absorption Re-emission Scattering) code to pre-compute X-ray spectra for various input parameters. The clumpy geometry has the benefit of describing eclipse events observed in X-ray spectra of some AGN (McKernan & Yaqoob 1998; Risaliti et al. 2002, 2005, 2009, 2011; Rivers et al. 2015; Marinucci et al. 2016; Ricci et al. 2016) and interfacing with infrared clumpy torus models (Nenkova et al. 2008a,b).

The geometry of the X-ray reprocessor is in part defined by σ_{TorUS} which sets the angular width of the cloud population: clouds are distributed along the equatorial plane for lower values of σ_{TorUS} and occupy nearly spherical coverage for the highest σ_{TorUS} values. σ_{TorUS} can range from 0° (no clumps) to 84° (spherical coverage). The fitted column density refers to the line-of-sight column density (N_{los}), which similar to the MYTORUS model in decoupled mode, measures the column of gas the X-ray photons transverse from the corona to the observer. The UXCLUMPY model partitions the sky around the X-ray source into bins of torus inclination angle and column density, such that similar inclination angles can have different line-of-sight column densities. $N_{\text{H,los}}$ drives the emergent X-ray spectral shape more than the inclination angle.

UXCLUMPY includes an optional inner uniform Compton-thick ring, where column densities exceed 10^{25} cm^{-2} , as a model component. This ring serves as a cold reflecting mirror with a covering factor that can range from 0 (no ring) to 0.6. Some heavily obscured, local AGN require this component to achieve a good fit to their $>10 \text{ keV}$ *NuSTAR* spectra (i.e., Circinus, NGC 424, and ESO 103-G035). Physically, such a component might represent a warped accretion disk or the inner wall of the torus (Buchner et al. 2019).

Table 5. MYTORUS Fit Parameters for Rejected Models: Scattered AGN Emission^a

Parameter	Coupled		Decoupled
Γ	$1.55^{+0.05}_{-0.03}$	$1.69^{+0.04}_{-0.08}$	$1.55^{+0.11}_{-0.12}$
Power law norm (10^{-4})	$1.43^{+0.17}_{-0.08}$	$0.93^{+0.34}_{-0.08}$	$1.39^{+0.52}_{-0.39}$
Inclination angle ($^{\circ}$)	$61.0^{+3.5}_{-0.6}$	$60.5^{+0.5}_{-0.2}$...
$N_{\text{H,equatorial}}$ (10^{24} cm^{-2})	$0.90^{+0.64}_{-0.47}$	$0.96^{+0.16}_{-0.26}$...
$N_{\text{H,los}}$ (10^{24} cm^{-2})	$0.21^{+0.04}_{-0.04}$
$N_{\text{H,global}}$ (10^{24} cm^{-2})	$1.00^{+1.20}_{-0.48}$
A_{S}^{b}	1 (f)	$7.9^{+3.0}_{-1.2}$	1 (f)
f_{scatt} (10^{-2})	17^{+3}_{-1}	27^{+2}_{-3}	18^{+6}_{-5}
χ^2 (dof)	364.0 (396)	338.6 (395)	360.0 (396)

^aIn the coupled realization of the MYTORUS model, the X-ray obscurer is assumed to be homogenous, with a fixed covering fraction of 0.5. The measured column density denotes the equatorial column density ($N_{\text{H,equatorial}}$). This table reports fit parameters where soft X-ray emission (0.5 - 2 keV) is modeled as originating from scattered AGN light.

^bNormalization between the transmitted AGN continuum and the Compton scattered and fluorescent line emission, which was either left frozen at unity or allowed to be free a parameter.

Table 6. MYTORUS Fit Parameters for Rejected Models: Jet Model^a

Parameter	Coupled		Decoupled
Γ_{AGN}	<1.49	<1.44	>2.44
Power law norm - AGN (10^{-4})	$1.04^{+0.10}_{-0.21}$	$0.53^{+0.07}_{-0.06}$	$85.5^{+5.8}_{-32.8}$
Γ_{Jet}	$1.62^{+0.15}_{-0.13}$	$1.86^{+0.24}_{-0.22}$	$1.84^{+0.37}_{-0.27}$
Power law norm - Jet (10^{-4})	$0.25^{+0.02}_{-0.01}$	0.26 ± 0.02	0.23 ± 0.02
Inclination angle ($^{\circ}$)	$60.9^{+2.8}_{-0.5}$	$60.5^{+0.5}_{-0.2}$...
$N_{\text{H,equatorial}}$ (10^{24} cm^{-2})	$0.80^{+0.50}_{-0.40}$	$0.60^{+0.10}_{-0.23}$...
$N_{\text{H,los}}$ (10^{24} cm^{-2})	$1.11^{+0.15}_{-0.16}$
$N_{\text{H,global}}$ (10^{24} cm^{-2})	$0.19^{+0.03}_{-0.06}$
A_{S}	1 (f)	$7.2^{+1.7}_{-2.4}$	1 (f)
χ^2 (dof)	363.4 (395)	335.0 (394)	350.4 (395)

^aThe fit parameters reported in this table are from modeling the soft X-ray emission with a jet origin.

^bNormalization between the transmitted AGN continuum and the Compton scattered and fluorescent line emission, which was either left frozen at unity or allowed to be free a parameter.

UXCLUMPY self-consistently models soft X-ray emission from scattered AGN light by accounting for the effects of reflection from hot gas (i.e., X-ray photons Compton scattered by hot electrons) and cold dense clouds beyond the

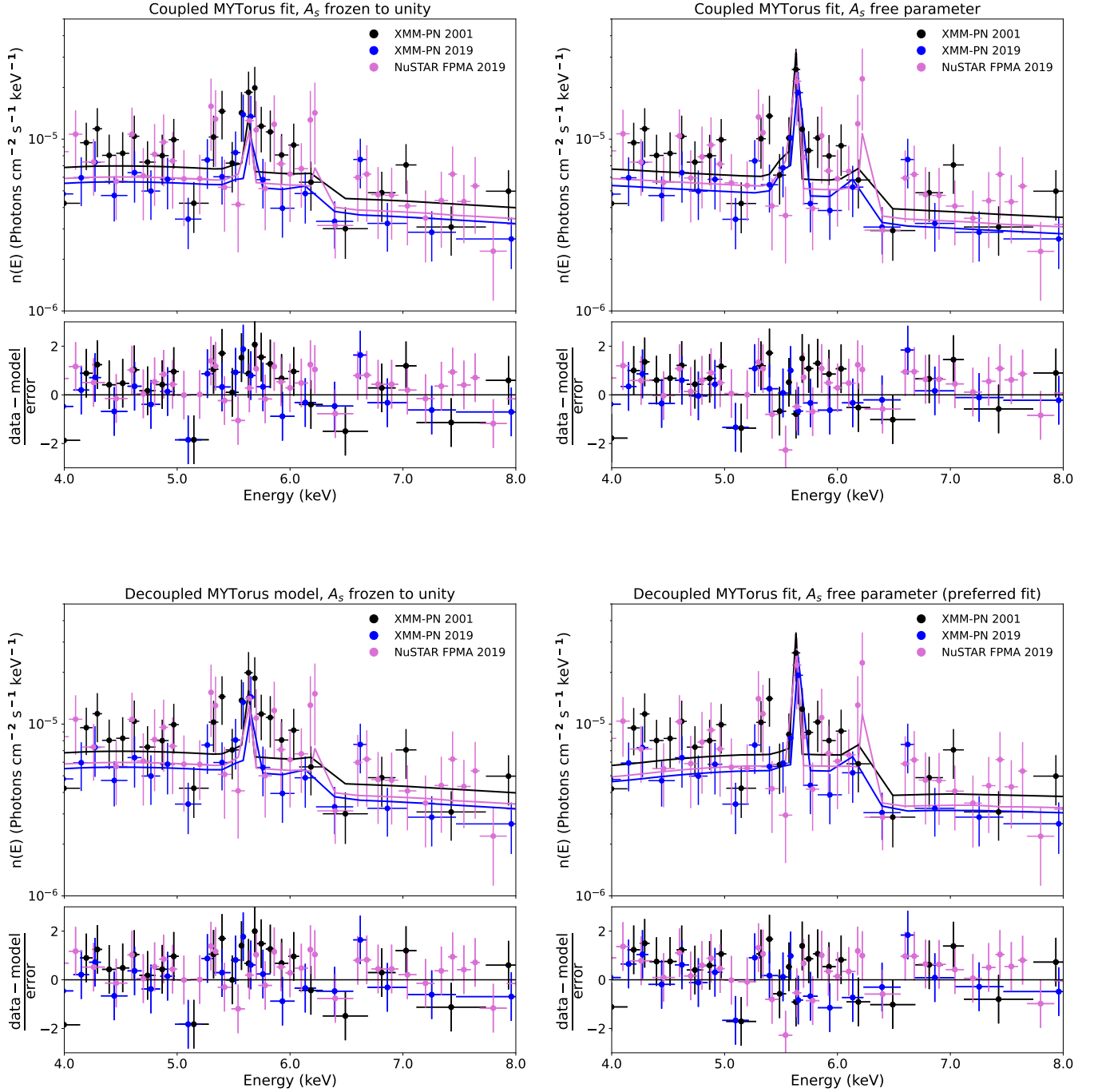


Figure 6. Close-up of the fitted Fe K α complex for various MYTORUS model realizations. Both the coupled and decoupled MYTORUS model fits where A_S was frozen at unity (left panels) exhibit significant residuals around the Fe K α line and local continuum. Though the coupled MYTORUS model where A_S was a free parameter (top right) shows a much better fit around the Fe K α complex, we reject this model fit due to the fitted grazing incidence angle of the torus (see Table 5). The fit to the Fe K α line and local continuum for our preferred model fit (decoupled MYTORUS scattered AGN model with A_S fitted as a free parameter) is shown in the bottom right for reference. Only a subset of the data are plotted for ease of visualization, though all spectra were fitted.

putative torus (which can give rise to Fe $K\alpha$ emission and a Compton hump; see e.g., [Bauer et al. 2015](#); [Fabbiano et al. 2017, 2018](#); [Jones et al. 2020](#); [Yi et al. 2021](#)). The UXCLUMPY-SCATTERED table model represents the angle-averaged spectrum of the warm reflected component whose model parameters are linked to those from the primary UXCLUMPY model to enforce self-consistency during spectral fitting. [Buchner et al. \(2019\)](#) advise that the relative normalization between the transmitted/Compton reflected and warm scattered models should not exceed 10% which would otherwise give rise to unphysical scattering efficiencies. The model is set up in XSPEC as:

$$\begin{aligned} \text{model} = & \text{const}_1 \times \text{phabs} \times \\ & (\text{atable}\{\text{uxclumpy} - \text{cutoff.fits}\} + \\ & \text{const}_2 \times \text{atable}\{\text{uxclumpy} - \text{cutoff} - \text{omni.fits}\}) \end{aligned}$$

where UXCLUMPY-CUTOFF.FITS models the transmitted and Compton reflected emission, UXCLUMPY-CUTOFF-OMNI.FITS models the warm scattered emission, and CONST_2 represents the scattering fraction (f_{scatt}). Similar to the MYTORUS modeling, CONST_1 parameterizes the cross-instrumental normalization and PHABS models the Galactic absorption and is frozen at this value ($1.46 \times 10^{20} \text{ cm}^{-2}$). We froze the high energy cutoff to the maximum allowed value of 400 keV as our data are not sensitive enough to measure this parameter.

When using this model configuration to fit the X-ray spectra of 3C 223, we initially imposed an upper limit on the scattering fraction of 0.1 (i.e., 10%), but this resulted in an unconstrained fit on the primary powerlaw continuum (i.e., the error on the powerlaw normalization spanned several orders of magnitude). We thus attempted two model realizations to fit the X-ray spectra of 3C 223 with UXCLUMPY: freezing the scattering fraction to 0.1 and allowing the scattering fraction to be a free parameter bounded by an upper limit of 1.0 (Table 7). We tested for the presence of an inner Compton-thick ring by allowing CTKcover to be a free parameter, but the best-fit covering factor was zero and we were only able to obtain upper limits.

Neither model realization is an adequate fit to the X-ray spectra of 3C 223. Similar to the rejected MYTORUS fits described in Appendix B, the Fe $K\alpha$ line is poorly accommodated by the UXCLUMPY model (see Figure 7). Allowing the scattering fraction to be a free parameter does improve the fit statistically compared with the fit where f_{scatt} is frozen at 10%, but the measured scattering fraction is unphysical, with a best-fit value pegged at the imposed limit of 100%, and the Fe $K\alpha$ line remains poorly fit by this model compared with the preferred model (see Figure 6, bottom right). The unphysical scattering fraction likely indicates that the soft emission has contributions beyond the scattering of the primary AGN emission that is not accommodated by the physical set-up of the model. Qualitatively, this result is similar to that of the MYTORUS model, where such additional physics is implicated by an elevated normalization factor between the transmitted and reflected component ($A_S \sim 5 - 6$), and the BORUS02 model with an elevated scattering fraction ($f_{\text{scatt}} = 27^{+5}_{-3}\%$). Both the UXCLUMPY model and MYTORUS scattered AGN model are consistent in finding heavy line-of-sight obscuration to the central engine ($N_H \geq 10^{23} \text{ cm}^{-2}$).

Table 7. UXCLUMPY Fit Parameters for Rejected Models^a

Parameter	Frozen f_{scatt}	Unconstrained f_{scatt}
Γ	$1.60^{+0.13}_{-0.10}$	$1.87^{+0.13}_{-0.10}$
Power law norm (10^{-4})	$5.30^{+0.65}_{-0.16}$	$3.26^{+1.70}_{-1.12}$
Inclination angle ($^{\circ}$)	<8	\dots^d
$N_{\text{H,los}}$ (10^{24} cm^{-2})	$0.18^{+0.06}_{-0.03}$	$0.31^{+0.07}_{-0.08}$
σ_{Torus} ($^{\circ}$) ^b	$14.1^{+1.7}_{-0.7}$	>70
CTKcover ^c	<0.20	<0.27
f_{scatt} (10^{-2})	10(f)	>66
χ^2 (dof)	361.8 (408)	351.7 (408)

^aWe present results for two realizations of using the UXCLUMPY model to fit the X-ray spectra of 3c223: freezing the scattering fraction (f_{scatt}) to the maximum advised limit of 10% (“Frozen f_{scatt} ”; Buchner et al. 2019) and allowing no limits on the scattering fraction other than a maximum value of unity (“Unconstrained f_{scatt} ”).

^b σ_{Torus} refers to the angular width of clouds in a clumpy torus, defining the torus scale height.

^cCTKcover parameterizes the covering factor of an inner Compton-thick ring of clouds ($N_{\text{H}} > 10^{25} \text{ cm}^{-2}$) around the corona.

^dThe best fit inclination angle was 90° , but the lower limit on this value was unconstrained, with a $\Delta\chi^2$ value of 0.4 for a 90% confidence interval for a 0° inclination angle.

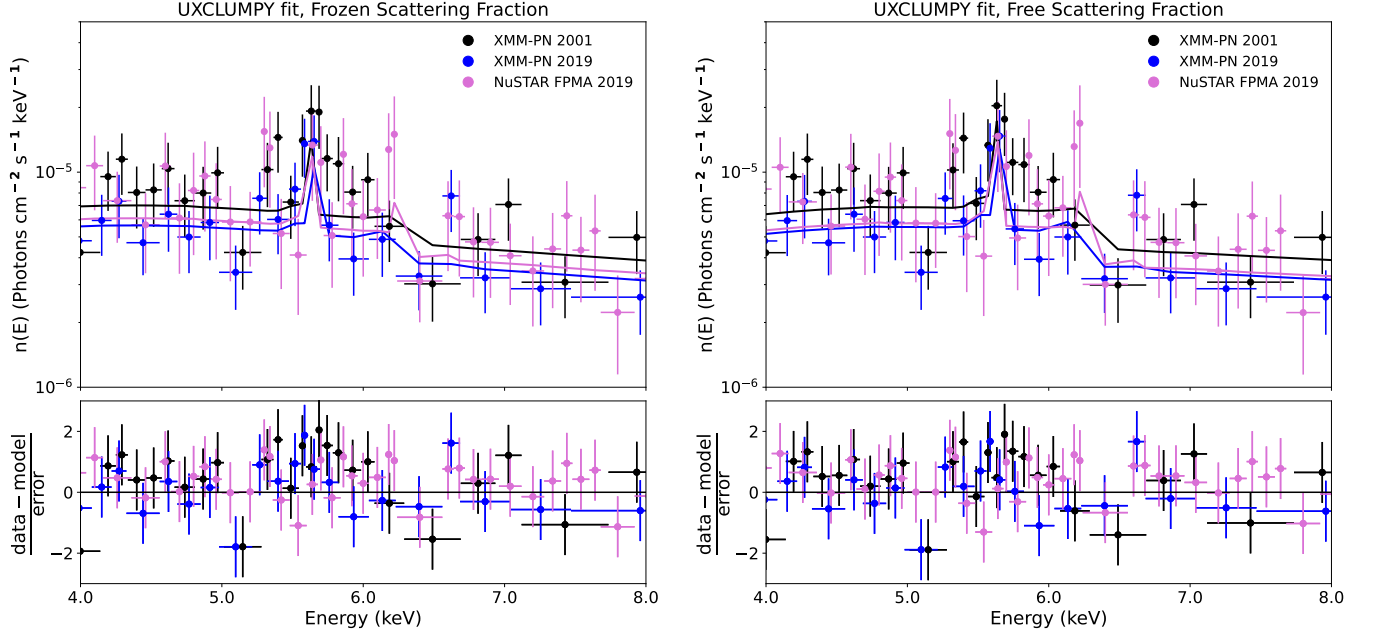


Figure 7. Close-up of the fitted Fe $K\alpha$ complex for UXCLUMPY model fits of the X-ray spectra of 3C 223 where (*left*) the scattering fraction is frozen to 10% and (*right*) the scattering fraction is a free parameter (with best-fit $f_{\text{scatt}} > 66\%$, which gives rise to an unphysically high scattering efficiency). In both cases, the Fe $K\alpha$ line is poorly fit, especially when compared with the accepted model (Figure 6, bottom right). For ease of visualization, just the *XMM-Newton* PN spectra and the *NuSTAR* FPMA spectrum are shown, though all 8 spectra from *XMM-Newton* (PN, MOS1, MOS2 from observations in 2001 and 2009) and *NuSTAR* (FPMA and FPMB) were fitted simultaneously.

D. ESTIMATING EXTINCTION-CORRECTED O III FLUX

Dust in the AGN Narrow Line Region (NLR) causes optical emission to suffer extinction. Such extinction is wavelength dependent, with bluer wavelengths being more extinguished than redder wavelength. This effect is described by extinction laws calibrated using measured fluxes of stars in the Milky Way (e.g., [Seaton 1979](#); [Cardelli et al. 1989](#)), Large Magellanic Cloud (e.g., [Howarth 1983](#); [Fitzpatrick 1986](#)), and Small Magellanic Cloud (e.g., [Prevot et al. 1984](#); [Bouchet et al. 1985](#)), or from the integrated emission of gas in external galaxies (e.g. [Calzetti et al. 1994, 2000](#)). The Balmer decrement, or the ratio of the observed $H\alpha$ to $H\beta$ flux compared to a theoretical value in the absence of extinction, provides a way to estimate and correct for the reddening of optical emission lines in the NLR.

For light embedded within a uniform dust layer, the observed flux (F_{obs}) is related to the intrinsic flux ($F_{\text{intrinsic}}$) by:

$$F_{\text{obs}} = F_{\text{intrinsic}} e^{-\tau(\lambda)}, \quad (\text{D1})$$

where $\tau(\lambda)$ is the (wavelength-dependent) optical depth. The difference in optical depth between the $H\alpha$ and $H\beta$ emission lines ($\tau_{H\beta} - \tau_{H\alpha}$) is then:

$$\tau_{H\beta} - \tau_{H\alpha} = \ln \left(\frac{F_{H\alpha,\text{obs}}/F_{H\beta,\text{obs}}}{F_{H\alpha,\text{intrinsic}}/F_{H\beta,\text{intrinsic}}} \right). \quad (\text{D2})$$

We take $F_{H\alpha,\text{intrinsic}}/F_{H\beta,\text{intrinsic}}$ to be 3.1, consistent with the temperatures and densities observed within the AGN NLR gas ([Osterbrock & Ferland 2006](#)).

We then use the [Cardelli et al. \(1989\)](#) extinction law ($k(\lambda)$) to estimate the level of extinction in the AGN NLR given this Balmer decrement. The [Cardelli et al. \(1989\)](#) extinction law has the form:

$$k(\lambda) = A(\lambda)/A(V) = a(x) + b(x)/R_V, \quad (\text{D3})$$

where $A(\lambda)$ is the extinction (in magnitudes) at any wavelength λ , $A(V)$ is the reference extinction in the V band, $R_V \equiv A(V)/E(B - V)$ (where $E(B - V)$ is the color excess due to reddening), and $a(x)$ and $b(x)$ are polynomials parameterizing the extinction law in units of $x = 1/\lambda$ (μm^{-1}) (see Equations 3a and 3b in [Cardelli et al. 1989](#), for the optical-near-infrared extinction law). In the [Cardelli et al. \(1989\)](#) model, $R_V = 3.1$. Since $A(\lambda)$ is measured in units of magnitude, i.e.,:

$$A(\lambda) = -2.5 \log \left(\frac{F_{\text{obs}}}{F_{\text{intrinsic}}} \right), \quad (\text{D4})$$

the relationship between extinction in magnitudes and optical depth is:

$$A(\lambda) = 1.086 \tau \quad (\text{D5})$$

Combining the above equations, $A(V)$ can be cast in terms of the extinction law and Balmer optical depth with the following:

$$A(V) = A(\lambda_{\text{Balmer decrement}})/k(\lambda_{\text{Balmer decrement}}) = \frac{1.086 (\tau_{H\beta} - \tau_{H\alpha})}{k(H\beta) - k(H\alpha)}, \quad (\text{D6})$$

where $k(H\beta)$ and $k(H\alpha)$ are the values of the [Cardelli et al. \(1989\)](#) extinction law at the wavelengths of $H\beta$ and $H\alpha$, respectively, giving:

$$A(V) = \frac{1.086 (\tau_{H\beta} - \tau_{H\alpha})}{1.164 - 0.818} = 3.14 (\tau_{H\beta} - \tau_{H\alpha}) = 3.14 \ln \left(\frac{F_{H\alpha,\text{obs}}/F_{H\beta,\text{obs}}}{3.1} \right). \quad (\text{D7})$$

Finally, we can measure the optical extinction at any wavelength with:

$$A(\lambda) = k(\lambda)A(V) = k(\lambda) \times 3.14 \ln \left(\frac{F_{H\alpha,\text{obs}}/F_{H\beta,\text{obs}}}{3.1} \right). \quad (\text{D8})$$

With $k(5007\text{\AA}) = 1.12$, the optical depth to the [O III] line is:

$$\tau_{5007\text{\AA}} = A(5007\text{\AA})/1.086 = 3.2 \ln \left(\frac{F_{H\alpha,\text{obs}}/F_{H\beta,\text{obs}}}{3.1} \right), \quad (\text{D9})$$

which provides the relation quoted in the main text of:

$$F_{[\text{O III}],\text{intrinsic}} = F_{[\text{O III}],\text{obs}} \left(\frac{F_{\text{H}\alpha,\text{obs}}/F_{\text{H}\beta,\text{obs}}}{3.1} \right)^{3.2}. \quad (\text{D10})$$

REFERENCES

- Akylas, A., Georgakakis, A., Georgantopoulos, I., et al. 2012, *A&A*, 546, A98. doi:10.1051/0004-6361/201219387
- Alexander, D. M., Stern, D., Del Moro, A., et al. 2013, *ApJ*, 773, 125. doi:10.1088/0004-637X/773/2/125
- Alonso-Herrero, A., Ward, M. J., & Kotilainen, J. K. 1997, *MNRAS*, 288, 977. doi:10.1093/mnras/288.4.977
- Ananna, T. T., Treister, E., Urry, C. M., et al. 2019, *ApJ*, 871, 240. doi:10.3847/1538-4357/aafb77
- Anders, E. & Grevesse, N. 1989, *GeoCoA*, 53, 197. doi:10.1016/0016-7037(89)90286-X
- Antonucci, R. 1993, *ARA&A*, 31, 473. doi:10.1146/annurev.aa.31.090193.002353
- Arnaud, K. A. 1996, *Astronomical Data Analysis Software and Systems V*, 101, 17
- Asmus, D., Gandhi, P., Hönig, S. F., et al. 2015, *MNRAS*, 454, 766. doi:10.1093/mnras/stv1950
- Baloković, M., Brightman, M., Harrison, F. A., et al. 2018, *ApJ*, 854, 42. doi:10.3847/1538-4357/aaa7eb
- Barret, D., Lam Trong, T., den Herder, J.-W., et al. 2018, *Proc. SPIE*, 10699, 106991G. doi:10.1117/12.2312409
- Bassani, L., Dadina, M., Maiolino, R., et al. 1999, *ApJS*, 121, 473. doi:10.1086/313202
- Bauer, F. E., Yan, L., Sajina, A., et al. 2010, *ApJ*, 710, 212. doi:10.1088/0004-637X/710/1/212
- Bauer, F. E., Arévalo, P., Walton, D. J., et al. 2015, *ApJ*, 812, 116. doi:10.1088/0004-637X/812/2/116
- Baum, S. A., Heckman, T. M., Bridle, A., et al. 1988, *ApJS*, 68, 643. doi:10.1086/191301
- Baumgartner, W. H., Tueller, J., Markwardt, C. B., et al. 2013, *ApJS*, 207, 19. doi:10.1088/0067-0049/207/2/19
- Best, P. N. & Heckman, T. M. 2012, *MNRAS*, 421, 1569. doi:10.1111/j.1365-2966.2012.20414.x
- Bettoni, D., Falomo, R., Fasano, G., et al. 2001, *A&A*, 380, 471. doi:10.1051/0004-6361:20011486
- Blandford, R. D. & Payne, D. G. 1982, *MNRAS*, 199, 883. doi:10.1093/mnras/199.4.883
- Blandford, R. D. & Znajek, R. L. 1977, *MNRAS*, 179, 433. doi:10.1093/mnras/179.3.433
- Bouchet, P., Lequeux, J., Maurice, E., et al. 1985, *A&A*, 149, 330
- Boorman, P. G., Gandhi, P., Baloković, M., et al. 2018, *MNRAS*, 477, 3775. doi:10.1093/mnras/sty861
- Brightman, M., Nandra, K., Salvato, M., et al. 2014, *MNRAS*, 443, 1999. doi:10.1093/mnras/stu1175
- Brightman, M. & Nandra, K. 2011, *MNRAS*, 413, 1206. doi:10.1111/j.1365-2966.2011.18207.x
- Buchner, J., Brightman, M., Nandra, K., et al. 2019, *A&A*, 629, A16. doi:10.1051/0004-6361/201834771
- Calzetti, D., Kinney, A. L., & Storchi-Bergmann, T. 1994, *ApJ*, 429, 582. doi:10.1086/174346
- Calzetti, D., Armus, L., Bohlin, R. C., et al. 2000, *ApJ*, 533, 682. doi:10.1086/308692
- Cardelli, J. A., Clayton, G. C., & Mathis, J. S. 1989, *ApJ*, 345, 245. doi:10.1086/167900
- Couto, G. S., Storchi-Bergmann, T., Siemiginowska, A., et al. 2020, *MNRAS*, 497, 5103. doi:10.1093/mnras/staa2268
- Croston, J. H., Birkinshaw, M., Hardcastle, M. J., et al. 2004, *MNRAS*, 353, 879. doi:10.1111/j.1365-2966.2004.08118.x
- Cutri, R. M., Wright, E. L., Conrow, T., et al. 2021, *VizieR Online Data Catalog*, II/328
- Daddi, E., Alexander, D. M., Dickinson, M., et al. 2007, *ApJ*, 670, 173. doi:10.1086/521820
- Donley, J. L., Koekemoer, A. M., Brusa, M., et al. 2012, *ApJ*, 748, 142. doi:10.1088/0004-637X/748/2/142
- Fabbiano, G., Elvis, M., Paggi, A., et al. 2017, *ApJL*, 842, L4. doi:10.3847/2041-8213/aa7551
- Fabbiano, G., Paggi, A., Siemiginowska, A., et al. 2018, *ApJL*, 869, L36. doi:10.3847/2041-8213/aaf73e
- Fabian, A. C. 2012, *ARA&A*, 50, 455. doi:10.1146/annurev-astro-081811-125521
- Fanaroff, B. L. & Riley, J. M. 1974, *MNRAS*, 167, 31P. doi:10.1093/mnras/167.1.31P
- Ferrarese, L. & Merritt, D. 2000, *ApJL*, 539, L9. doi:10.1086/312838
- Fitzpatrick, E. L. 1986, *AJ*, 92, 1068. doi:10.1086/114237
- Fruscione, A., McDowell, J. C., Allen, G. E., et al. 2006, *Proc. SPIE*, 6270, 62701V. doi:10.1117/12.671760
- Fürst, F., Müller, C., Madsen, K. K., et al. 2016, *ApJ*, 819, 150. doi:10.3847/0004-637X/819/2/150
- Gandhi, P., Horst, H., Smette, A., et al. 2009, *A&A*, 502, 457. doi:10.1051/0004-6361/200811368
- Gandhi, P., Lansbury, G. B., Alexander, D. M., et al. 2014, *ApJ*, 792, 117. doi:10.1088/0004-637X/792/2/117

- Gandhi, P., Hönig, S. F., & Kishimoto, M. 2015, *ApJ*, 812, 113. doi:10.1088/0004-637X/812/2/113
- Gandhi, P., Annun, A., Lansbury, G. B., et al. 2017, *MNRAS*, 467, 4606. doi:10.1093/mnras/stx357
- Ghisellini, G., Haardt, F., & Matt, G. 1994, *MNRAS*, 267, 743. doi:10.1093/mnras/267.3.743
- Gilli, R., Comastri, A., & Hasinger, G. 2007, *A&A*, 463, 79. doi:10.1051/0004-6361:20066334
- Guainazzi, M., Siemiginowska, A., Rodriguez-Pascual, P., et al. 2004, *A&A*, 421, 461. doi:10.1051/0004-6361:20047051
- Guainazzi, M. & Bianchi, S. 2007, *MNRAS*, 374, 1290. doi:10.1111/j.1365-2966.2006.11229.x
- Haardt, F. & Maraschi, L. 1991, *ApJL*, 380, L51. doi:10.1086/186171
- Hardcastle, M. J., Evans, D. A., & Croston, J. H. 2006, *MNRAS*, 370, 1893. doi:10.1111/j.1365-2966.2006.10615.x
- Hardcastle, M. J., Evans, D. A., & Croston, J. H. 2007, *MNRAS*, 376, 1849. doi:10.1111/j.1365-2966.2007.11572.x
- Hardcastle, M. J., Evans, D. A., & Croston, J. H. 2009, *MNRAS*, 396, 1929. doi:10.1111/j.1365-2966.2009.14887.x
- Harrison, F. A., Craig, W. W., Christensen, F. E., et al. 2013, *ApJ*, 770, 103. doi:10.1088/0004-637X/770/2/103
- Heckman, T. M. & Best, P. N. 2014, *ARA&A*, 52, 589. doi:10.1146/annurev-astro-081913-035722
- Heckman, T. M., Ptak, A., Hornschemeier, A., et al. 2005, *ApJ*, 634, 161. doi:10.1086/491665
- Hickox, R. C. & Alexander, D. M. 2018, *ARA&A*, 56, 625. doi:10.1146/annurev-astro-081817-051803
- Hine, R. G. & Longair, M. S. 1979, *MNRAS*, 188, 111. doi:10.1093/mnras/188.1.111
- Ho, L. C., Filippenko, A. V., & Sargent, W. L. W. 1997, *ApJS*, 112, 315. doi:10.1086/313041
- Holt, J., Tadhunter, C. N., & Morganti, R. 2008, *MNRAS*, 387, 639. doi:10.1111/j.1365-2966.2008.13089.x
- Hönig, S. F., Kishimoto, M., Gandhi, P., et al. 2010, *A&A*, 515, A23. doi:10.1051/0004-6361/200913742
- Hopkins, P. F., Hernquist, L., Cox, T. J., et al. 2008, *ApJS*, 175, 356. doi:10.1086/524362
- Hopkins, P. F., Richards, G. T., & Hernquist, L. 2007, *ApJ*, 654, 731. doi:10.1086/509629
- Hopkins, P. F., Hernquist, L., Cox, T. J., et al. 2006, *ApJS*, 163, 1. doi:10.1086/499298
- Horst, H., Gandhi, P., Smette, A., et al. 2008, *A&A*, 479, 389. doi:10.1051/0004-6361:20078548
- Howarth, I. D. 1983, *MNRAS*, 203, 301. doi:10.1093/mnras/203.2.301
- Jia, J., Ptak, A., Heckman, T., et al. 2013, *ApJ*, 777, 27. doi:10.1088/0004-637X/777/1/27
- Jones, M. L., Fabbiano, G., Elvis, M., et al. 2020, *ApJ*, 891, 133. doi:10.3847/1538-4357/ab76c8
- Kauffmann, G., Heckman, T. M., Tremonti, C., et al. 2003, *MNRAS*, 346, 1055. doi:10.1111/j.1365-2966.2003.07154.x
- Koss, M., Trakhtenbrot, B., Ricci, C., et al. 2017, *ApJ*, 850, 74. doi:10.3847/1538-4357/aa8ec9
- Krolik, J. H., Madau, P., & Zycki, P. T. 1994, *ApJL*, 420, L57. doi:10.1086/187162
- Kuźmierz, A., Jamroz, M., Bronarska, K., et al. 2018, *ApJS*, 238, 9. doi:10.3847/1538-4365/aad9ff
- LaMassa, S. M., Heckman, T. M., Ptak, A., et al. 2009, *ApJ*, 705, 568. doi:10.1088/0004-637X/705/1/568
- LaMassa, S. M., Heckman, T. M., Ptak, A., et al. 2010, *ApJ*, 720, 786. doi:10.1088/0004-637X/720/1/786
- LaMassa, S. M., Heckman, T. M., Ptak, A., et al. 2011, *ApJ*, 729, 52. doi:10.1088/0004-637X/729/1/52
- LaMassa, S. M., Heckman, T. M., & Ptak, A. 2012, *ApJ*, 758, 82. doi:10.1088/0004-637X/758/2/82
- LaMassa, S. M., Yaqoob, T., Ptak, A. F., et al. 2014, *ApJ*, 787, 61. doi:10.1088/0004-637X/787/1/61
- LaMassa, S. M., Ricarte, A., Glikman, E., et al. 2016, *ApJ*, 820, 70. doi:10.3847/0004-637X/820/1/70
- LaMassa, S. M., Yaqoob, T., & Kilgard, R. 2017, *ApJ*, 840, 11. doi:10.3847/1538-4357/aa68df
- LaMassa, S. M., Yaqoob, T., Boorman, P. G., et al. 2019, *ApJ*, 887, 173. doi:10.3847/1538-4357/ab552c
- Lamastra, A., Bianchi, S., Matt, G., et al. 2009, *A&A*, 504, 73. doi:10.1051/0004-6361/200912023
- Lansbury, G. B., Alexander, D. M., Del Moro, A., et al. 2014, *ApJ*, 785, 17. doi:10.1088/0004-637X/785/1/17
- Lansbury, G. B., Gandhi, P., Alexander, D. M., et al. 2015, *ApJ*, 809, 115. doi:10.1088/0004-637X/809/2/115
- Lawrence, A. & Elvis, M. 1982, *ApJ*, 256, 410. doi:10.1086/159918
- Levenson, N. A., Radomski, J. T., Packham, C., et al. 2009, *ApJ*, 703, 390. doi:10.1088/0004-637X/703/1/390
- Liu, X., Zakamska, N. L., Greene, J. E., et al. 2009, *ApJ*, 702, 1098. doi:10.1088/0004-637X/702/2/1098
- Lusso, E., Comastri, A., Vignali, C., et al. 2010, *A&A*, 512, A34. doi:10.1051/0004-6361/200913298
- Lusso, E., Comastri, A., Simmons, B. D., et al. 2012, *MNRAS*, 425, 623. doi:10.1111/j.1365-2966.2012.21513.x
- Lutz, D., Maiolino, R., Spoon, H. W. W., et al. 2004, *A&A*, 418, 465. doi:10.1051/0004-6361:20035838
- Madrid, J. P., Chiaberge, M., Floyd, D., et al. 2006, *ApJS*, 164, 307. doi:10.1086/504480
- Madsen, K. K., Beardmore, A. P., Forster, K., et al. 2017, *AJ*, 153, 2. doi:10.3847/1538-3881/153/1/2
- Marchesi, S., Ajello, M., Marcotulli, L., et al. 2018, *ApJ*, 854, 49. doi:10.3847/1538-4357/aaa410
- Marchesi, S., Ajello, M., Zhao, X., et al. 2019, *ApJ*, 872, 8. doi:10.3847/1538-4357/aafbeb

- Marconi, A., Risaliti, G., Gilli, R., et al. 2004, *MNRAS*, 351, 169. doi:10.1111/j.1365-2966.2004.07765.x
- Marinucci, A., Bianchi, S., Matt, G., et al. 2016, *MNRAS*, 456, L94. doi:10.1093/mnras/ltv178
- Massaro, F., Tremblay, G. R., Harris, D. E., et al. 2012, *ApJS*, 203, 31. doi:10.1088/0067-0049/203/2/31
- Mateos, S., Carrera, F. J., Barcons, X., et al. 2017, *ApJL*, 841, L18. doi:10.3847/2041-8213/aa7268
- Matt, G., Brandt, W. N., & Fabian, A. C. 1996, *MNRAS*, 280, 823. doi:10.1093/mnras/280.3.823
- McKernan, B. & Yaqoob, T. 1998, *ApJL*, 501, L29. doi:10.1086/311457
- Merloni, A., Bongiorno, A., Brusa, M., et al. 2014, *MNRAS*, 437, 3550. doi:10.1093/mnras/stt2149
- Mulchaey, J. S., Koratkar, A., Ward, M. J., et al. 1994, *ApJ*, 436, 586. doi:10.1086/174933
- Murphy, K. D. & Yaqoob, T. 2009, *MNRAS*, 397, 1549. doi:10.1111/j.1365-2966.2009.15025.x
- Nenkova, M., Sirocky, M. M., Ivezić, Ž., et al. 2008, *ApJ*, 685, 147. doi:10.1086/590482
- Nenkova, M., Sirocky, M. M., Nikutta, R., et al. 2008, *ApJ*, 685, 160. doi:10.1086/590483
- Nesvadba, N. P. H., Lehnert, M. D., De Breuck, C., et al. 2008, *A&A*, 491, 407. doi:10.1051/0004-6361:200810346
- Netzer, H. 2015, *ARA&A*, 53, 365. doi:10.1146/annurev-astro-082214-122302
- Orrù, E., Murgia, M., Feretti, L., et al. 2010, *A&A*, 515, A50. doi:10.1051/0004-6361/200913837
- Osterbrock, D. E. & Ferland, G. J. 2006, *Astrophysics of gaseous nebulae and active galactic nuclei*, 2nd. ed. by D.E. Osterbrock and G.J. Ferland. Sausalito, CA: University Science Books, 2006
- Panessa, F., Bassani, L., Cappi, M., et al. 2006, *A&A*, 455, 173. doi:10.1051/0004-6361:20064894
- Panessa, F., Bassani, L., Landi, R., et al. 2016, *MNRAS*, 461, 3153. doi:10.1093/mnras/stw1438
- Planck Collaboration, Ade, P. A. R., Aghanim, N., et al. 2016, *A&A*, 594, A13. doi:10.1051/0004-6361/201525830
- Prevot, M. L., Lequeux, J., Maurice, E., et al. 1984, *A&A*, 132, 389
- Ramos Almeida, C., Pérez García, A. M., Acosta-Pulido, J. A., et al. 2007, *AJ*, 134, 2006. doi:10.1086/522625
- Reeves, J. N. & Turner, M. J. L. 2000, *MNRAS*, 316, 234. doi:10.1046/j.1365-8711.2000.03510.x
- Reyes, R., Zakamska, N. L., Strauss, M. A., et al. 2008, *AJ*, 136, 2373. doi:10.1088/0004-6256/136/6/2373
- Reynolds, C. S., Lohfink, A. M., Ogle, P. M., et al. 2015, *ApJ*, 808, 154. doi:10.1088/0004-637X/808/2/154
- Ricci, C., Trakhtenbrot, B., Koss, M. J., et al. 2017, *Nature*, 549, 488. doi:10.1038/nature23906
- Ricci, C., Bauer, F. E., Arevalo, P., et al. 2016, *ApJ*, 820, 5. doi:10.3847/0004-637X/820/1/5
- Ricci, C., Ueda, Y., Koss, M. J., et al. 2015, *ApJL*, 815, L13. doi:10.1088/2041-8205/815/1/L13
- Risaliti, G., Elvis, M., & Nicastro, F. 2002, *ApJ*, 571, 234. doi:10.1086/324146
- Risaliti, G., Elvis, M., Fabbiano, G., et al. 2005, *ApJL*, 623, L93. doi:10.1086/430252
- Risaliti, G., Salvati, M., Elvis, M., et al. 2009, *MNRAS*, 393, L1. doi:10.1111/j.1745-3933.2008.00580.x
- Risaliti, G., Nardini, E., Salvati, M., et al. 2011, *MNRAS*, 410, 1027. doi:10.1111/j.1365-2966.2010.17503.x
- Rivers, E., Risaliti, G., Walton, D. J., et al. 2015, *ApJ*, 804, 107. doi:10.1088/0004-637X/804/2/107
- Sambruna, R. M. & Eracleous, M. 2001, *X-ray Astronomy: Stellar Endpoints, AGN, and the Diffuse X-ray Background*, 599, 355. doi:10.1063/1.1434648
- Sanders, D. B., Soifer, B. T., Elias, J. H., et al. 1988, *ApJ*, 325, 74. doi:10.1086/165983
- Seaton, M. J. 1979, *MNRAS*, 187, 73. doi:10.1093/mnras/187.1.73P
- Shakura, N. I. & Sunyaev, R. A. 1973, *A&A*, 500, 33
- Siemiginowska, A., Stawarz, L., Cheung, C. C., et al. 2012, *ApJ*, 750, 124. doi:10.1088/0004-637X/750/2/124
- Sobolewska, M., Siemiginowska, A., Guainazzi, M., et al. 2019, *ApJ*, 871, 71. doi:10.3847/1538-4357/aaee78
- Sobolewska, M. A., Siemiginowska, A., Migliori, G., et al. 2012, *ApJ*, 758, 90. doi:10.1088/0004-637X/758/2/90
- Sobolewska, M., Siemiginowska, A., Guainazzi, M., et al. 2019, *ApJ*, 884, 166. doi:10.3847/1538-4357/ab3ec3
- Stern, D. 2015, *ApJ*, 807, 129. doi:10.1088/0004-637X/807/2/129
- Tozzi, P., Gilli, R., Mainieri, V., et al. 2006, *A&A*, 451, 457. doi:10.1051/0004-6361:20042592
- Treister, E., Urry, C. M., & Virani, S. 2009, *ApJ*, 696, 110. doi:10.1088/0004-637X/696/1/110
- Tremaine, S., Gebhardt, K., Bender, R., et al. 2002, *ApJ*, 574, 740. doi:10.1086/341002
- Turner, T. J., George, I. M., Nandra, K., et al. 1997, *ApJ*, 488, 164. doi:10.1086/304701
- Turner, T. J. & Miller, L. 2009, *A&A Rv*, 17, 47. doi:10.1007/s00159-009-0017-1
- Tzanavaris, P., Yaqoob, T., LaMassa, S., et al. 2021, *ApJ*, 922, 85. doi:10.3847/1538-4357/ac1ff6
- Tzanavaris, P., Yaqoob, T., LaMassa, S., et al. 2019, *ApJ*, 885, 62. doi:10.3847/1538-4357/ab4282
- Ueda, Y., Akiyama, M., Ohta, K., et al. 2003, *ApJ*, 598, 886. doi:10.1086/378940
- Ueda, Y., Akiyama, M., Hasinger, G., et al. 2014, *ApJ*, 786, 104. doi:10.1088/0004-637X/786/2/104

- Urry, C. M. & Padovani, P. 1995, *PASP*, 107, 803.
doi:10.1086/133630
- Ursini, F., Bassani, L., Panessa, F., et al. 2018, *MNRAS*, 474, 5684. doi:10.1093/mnras/stx3159
- van Breugel, W. J. M., Heckman, T. M., Miley, G. K., et al. 1986, *ApJ*, 311, 58. doi:10.1086/164754
- Vasudevan, R. V. & Fabian, A. C. 2007, *MNRAS*, 381, 1235. doi:10.1111/j.1365-2966.2007.12328.x
- Verner, D. A., Ferland, G. J., Korista, K. T., et al. 1996, *ApJ*, 465, 487. doi:10.1086/177435
- Vignali, C., Alexander, D. M., & Comastri, A. 2006, *MNRAS*, 373, 321. doi:10.1111/j.1365-2966.2006.11033.x
- Vignali, C., Alexander, D. M., Gilli, R., et al. 2010, *MNRAS*, 404, 48. doi:10.1111/j.1365-2966.2010.16275.x
- Winter, L. M., Mushotzky, R. F., Reynolds, C. S., et al. 2009, *ApJ*, 690, 1322. doi:10.1088/0004-637X/690/2/1322
- Woo, J.-H. & Urry, C. M. 2002, *ApJ*, 579, 530. doi:10.1086/342878
- Worsley, M. A., Fabian, A. C., Bauer, F. E., et al. 2005, *MNRAS*, 357, 1281. doi:10.1111/j.1365-2966.2005.08731.x
- Wright, E. L., Eisenhardt, P. R. M., Mainzer, A. K., et al. 2010, *AJ*, 140, 1868. doi:10.1088/0004-6256/140/6/1868
- Yaqoob, T., McKernan, B., Done, C., et al. 1993, *ApJL*, 416, L5. doi:10.1086/187057
- Yaqoob, T., George, I. M., Nandra, K., et al. 1999, *ApJL*, 525, L9. doi:10.1086/312327
- Yaqoob, T. & Murphy, K. D. 2011, *MNRAS*, 412, 835. doi:10.1111/j.1365-2966.2010.17942.x
- Yaqoob, T. 2012, *MNRAS*, 423, 3360. doi:10.1111/j.1365-2966.2012.21129.x
- Yaqoob, T., Tatum, M. M., Scholtes, A., et al. 2015, *MNRAS*, 454, 973. doi:10.1093/mnras/stv2021
- Yi, H., Wang, J., Shu, X., et al. 2021, *ApJ*, 908, 156. doi:10.3847/1538-4357/abcec3
- Zakamska, N. L., Strauss, M. A., Krolik, J. H., et al. 2003, *AJ*, 126, 2125. doi:10.1086/378610
- Zhao, X., Marchesi, S., Ajello, M., et al. 2021, *A&A*, 650, A57. doi:10.1051/0004-6361/202140297